Probing signatures of fractionalization in the candidate quantum spin liquid Cu_2IrO_3 via anomalous Raman scattering

Srishti Pal,[1] Arnab Seth,[2] Piyush Sakrikar,[3] Anzar Ali,[3] Subhro Bhattacharjee,[2] D. V. S. Muthu,[1] Yogesh Singh,[3] and A. K. Sood[1,*]

[1]*Department of Physics, Indian Institute of Science, Bengaluru 560012, India*

[2]*International Centre for Theoretical Sciences, Tata Institute of Fundamental Research, Bengaluru 560089, India*

[3]*Indian Institute of Science Education and Research (IISER) Mohali, Knowledge City, Sector 81, Mohali 140306, India*

(Received 1 June 2021; revised 3 July 2021; accepted 5 November 2021; published 17 November 2021)

Long-range entanglement in quantum spin liquids (QSLs) leads to novel low-energy excitations with fractionalized quantum numbers and (in two dimensions) statistics. Experimental detection and manipulation of these excitations present a challenge particularly in view of diverse candidate magnets. A promising probe of fractionalization is their coupling to phonons. Here, we present Raman scattering results for the $S = 1/2$ honeycomb iridate Cu_2IrO_3, a candidate Kitaev QSL with fractionalized Majorana fermions and Ising flux excitations. We observe anomalous low-temperature frequency shift and linewidth broadening of the Raman intensities in addition to a broad magnetic continuum, both of which, as we derive, are naturally attributed to the phonon decaying into itinerant Majoranas. The dynamic Raman susceptibility marks a crossover from the QSL to a thermal paramagnet at ∼120 K. The phonon anomalies below this temperature demonstrate a strong phonon-Majorana coupling. These results provide evidence of spin fractionalization in Cu_2IrO_3.

DOI: 10.1103/PhysRevB.104.184420

I. INTRODUCTION

Recent advances in condensed matter physics and materials science have shown that several so-called *elementary particles*, originally conceived in the context of high-energy physics, can emerge as low-energy excitations (quasiparticles) in condensed matter systems. In addition to providing an impetus to the paradigm of emergent quantum phenomena [1–3], these materials then provide concrete contexts to understand the properties of these novel excitations and the settings for their emergence as an interplay of symmetries and many-body entanglement. This ranges from the weakly correlated physics of Dirac fermions in monolayer graphene [4,5] and Weyl fermions in topological semimetals [6–8], on the one hand, to the strongly correlated fractionalized excitations in fractional quantum Hall systems [9,10], on the other.

In this context, the possibility of emergence of the elusive (in high-energy particle physics) Majorana fermion [11,12] in several candidate solid-state systems such as topological superconductors [13–17], fractional quantum Hall systems [18], and quantum spin liquids (QSLs) [19–22] has been invoked to account for startling novel low-energy properties of these systems. Among them, the Kitaev QSL [19] on the isotropic honeycomb lattice provides a unique opportunity where propagating Majorana excitations coupled to emergent Z_2 fluxes arise due to the long-range quantum entanglement present in the system resulting in the fractionalization of the underlying microscopic spin-$\frac{1}{2}$'s [19].

Our present understanding suggests that a key ingredient in realizing Kitaev physics is specific *compass* spin-spin interactions [23,24] on a tricoordinated motif consisting of edge-sharing octahedra [23,25]. Our growing understanding of magnets with strong spin-orbit coupling has provided a slew of such candidate Kitaev QSL materials containing $4d$ and $5d$ transition metal ions. The most notable ones among these are Na_2IrO_3 [26] and α-$RuCl_3$ [27] on a two-dimensional layered honeycomb motif and γ- and β-Li_2IrO_3 [28] on a three-dimensional hyperhoneycomb lattice. A combination of thermodynamic measurements and scattering experiments [21,29] on these "first-generation" Kitaev materials show extremely interesting finite-temperature behavior including possible signatures of fractionalization and thereby raise questions about their proximity to Kitaev (or other) QSLs [20,21,30]. However, they ultimately order magnetically at a much lower temperature possibly due to additional non-Kitaev interactions in these systems. Thus, while the above compounds are very interesting in their own rights to understand the possible interplay of magnetic fluctuations and fractionalization, the realization of the Kitaev QSL with pristine signatures of the fractionalized Majoranas still remains an open issue.

In this paper, we report our results on the Raman scattering and magnetoelastic coupling of the "second-generation" Kitaev material Cu_2IrO_3 [31], where the magnetic order is absent suggesting the possibility of smaller non-Kitaev interactions. In particular, despite a Curie-Weiss temperature and effective magnetic moment similar to Na_2IrO_3, muon spin relaxation (μSR) and specific heat studies on Cu_2IrO_3 have shown an absence of magnetic order and an excitation spectrum dominated by low-energy Ir spin dynamics [32,33]. The correlated nature of this low-temperature dynamic paramagnet is further supported by the nuclear quadrupole resonance (NQR) measurements [34]. These

*asood@iisc.ac.in

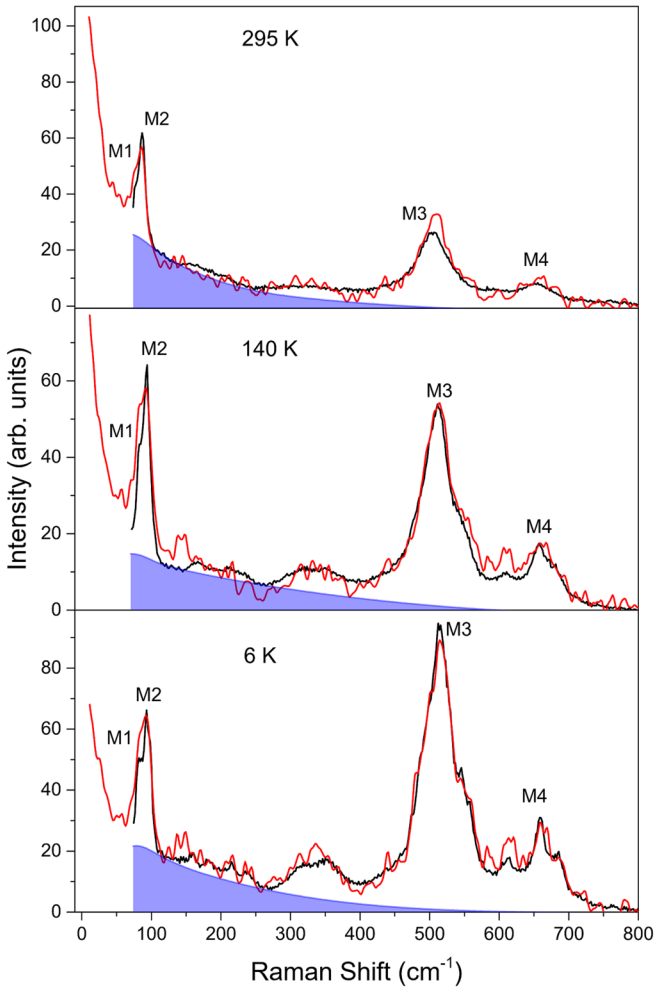

FIG. 1. Black and red curves represent the unpolarized and cross-polarized Raman spectra of Cu_2IrO_3 at three different temperatures in the spectral ranges of 70–800 cm^{-1} and 10–800 cm^{-1}, respectively. The shaded region represents the low-energy magnetic continuum.

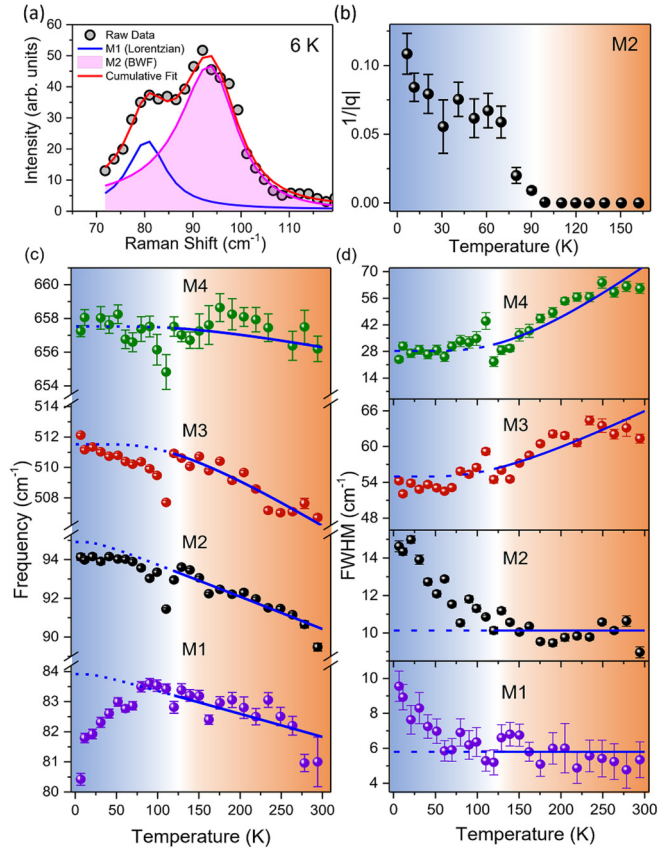

FIG. 2. (a) Phonon fits of the M1-M2 doublet with Lorentzian and Breit-Wigner-Fano (BWF) line shapes, respectively. (b) Temperature evolution of the asymmetry parameter $1/|q|$ of the M2 mode. Temperature dependence of (c) phonon frequency and (d) FWHM. Blue curves are anharmonic fits to phonon frequencies and FWHMs. Shaded regions demonstrate the boundary between the normal and the Kitaev paramagnetic states.

findings suggest that Cu_2IrO_3 may offer an ideal playground to investigate fractionalization in a Kitaev QSL with an eye towards positive characterization of the Majorana fermions therein. Such Majorana fermions can then couple to the optical phonons through the regular spin-phonon coupling leading to their characteristic experimental signatures. Incidentally, such coupling has only been studied for the acoustic phonons for a Kitaev QSL [35–37].

Indeed, strong spin-orbit coupling results in intricate mixing of the real and spin space. Thus, on generic grounds, one expects these compounds to have enhanced spin-lattice coupling. Can this spin-(optical-)phonon coupling, as probed in Raman scattering, then lead to positive identification of the possible fractionalized excitations (Majorana fermions in a Kitaev QSL) in candidate QSL materials such as Cu_2IrO_3? The central result of our work is the anomalous shift and broadening of the Raman-active phonons in Cu_2IrO_3 (Fig. 2), which indicate that extra decay channels become active at low temperatures for the low-energy Raman-active phonons. In the absence of magnetic order, natural candidates for coherent modes that can result in phonon decay, within Kitaev phenomenology, are itinerant Majorana fermions. Indeed, we find that such fractionalization does provide a successful explanation for our Raman measurements. Our estimate of the Kitaev exchange from the band edge of the magnetic continuum is consistent with earlier NQR measurements. The temperature dependence of Raman susceptibility is nonmonotonic and clearly evidences fermionic Majorana excitations prevailing over a conventional bosonic background below about 120 K.

The second-generation Kitaev materials, such as Cu_2IrO_3, are obtained by partially or fully replacing the alkali atoms in α-A_2IrO_3 with other atoms. Incredibly, the new materials produced in this manner, $H_3LiIr_2O_6$ [38], Cu_2IrO_3 [31], and $Ag_3LiIr_2O_6$ [39], have been shown to be QSL candidates with no signatures of magnetic order using various thermodynamic and dynamic probes [32,34,38,39]. In these second-generation Kitaev materials, the edge-sharing IrO_6 octahedra forming a honeycomb lattice plane are retained. However, the interplanar connectivity is changed. For example, Cu_2IrO_3 crystallizes in the same $C2/c$ monoclinic structure as Na_2IrO_3. The honeycomb layers are formed by an edge-sharing $(Ir_{2/3}Cu_{1/3})O_6$ octahedral arrangement identical to Na_2IrO_3, but the interlayer connections via distorted NaO_6

octahedra are replaced by linear CuO_2 dumbbells resulting in a larger c axis. This enhanced two-dimensional (2D) character of the honeycomb layers, along with the proximity of the Ir-Ir-Ir angles towards the ideal value of 120° compared with its predecessor Na_2IrO_3, puts copper iridate closer to the ideal Kitaev limit. Similar interlayer bonding is found for $H_3LiIr_2O_6$ [38] and $Ag_3LiIr_2O_6$ [39].

The nature of the synthesis makes these second-generation Kitaev materials prone to disorder. Examples include proton positional disorder in $H_3LiIr_2O_6$, Ag positional disorder in $Ag_3LiIr_2O_6$, and Cu mixed valent disorder in Cu_2IrO_3. The possible role of disorder in stabilizing the QSL in these materials has been discussed recently [32,38,40–42]. In the context of Raman measurements, the proton disorder in $H_3LiIr_2O_6$ has been suggested to lead to the observed anomalously broad phonon modes as well as the weak fermionic contribution to the magnetic continuum [43]. Unlike $H_3LiIr_2O_6$, however, the synthesis of $Ag_3LiIr_2O_6$ and Cu_2IrO_3 can be controlled to reduce the disorder. For example, while disordered $Ag_3LiIr_2O_6$ samples with Ag randomly occupying voids of the $LiIr_2O_6$ honeycomb layers show broad features in the heat capacity at low temperatures, higher-quality samples which do not have this Ag positional disorder actually undergo long-ranged magnetic order [44]. For Cu_2IrO_3 as well, disorder can lead to measurable consequences. Initial reports observed a glassy state at low temperatures ($T \sim 3.5$ K) using magnetic susceptibility [31]. A careful experimental and theoretical study including x-ray absorption spectroscopy, μSR, and density functional theory identified the source of disorder as an 8.5–13% contamination of Cu^{2+} instead of Cu^{+} in Cu_2IrO_3 [33]. The Cu^{2+} spins were found to be located within the voids of the honeycomb layers formed by the edge-sharing IrO_6 octahedra. From μSR, the Cu^{2+} spins were found to be responsible for the spin-glass freezing, while the Ir^{4+} honeycomb sublattice was found to be in a dynamically fluctuating QSL-like state. Additionally, the frozen regions and the QSL regions were found to occupy different volume fractions of the sample. Thus it is clear that a majority (∼90%) of the disordered Cu_2IrO_3 sample is actually in a QSL state and the frozen volume fraction is phase separated from the QSL part of the material [33].

Subsequently, we have been able to synthesize high-quality Cu_2IrO_3 samples—used for the present experiments—which do not show any features of a glassy state in ac magnetic susceptibility [see Fig. 7(d)]. This strongly suggests that our Cu_2IrO_3 samples have a much smaller amount of disorder. This is confirmed by microscopic probes of magnetism, such as μSR, which show an absence of any static magnetism down to 260 mK in the present samples [32]. These measurements additionally show that the Ir spins stay in a dynamically fluctuating QSL-like state down to temperatures more than two orders of magnitude smaller than the Curie-Weiss temperature [32]. Even in our higher-quality samples, however, some small amount of disorder remains, as evidenced by the low-temperature ($T \leqslant 20$ K) sub-Curie-law susceptibility [see Figs. 7(c) and 7(e)] and scaling behaviors in various thermodynamic quantities, which is consistent with a small fraction of random singlets in the background of a QSL-like phase [32,45]. The absence of freezing in our samples suggests a smaller concentration of Cu^{2+} impurities. Analysis of the low-temperature susceptibility demonstrates that ≈5% of $S = 1/2$ impurities can explain the low-temperature sub-Curie law (see Appendix A).

We have therefore chosen the second-generation Kitaev material Cu_2IrO_3 to study the fractionalization predicted for a Kitaev QSL: Most prominently, the itinerant Majorana fermions [46]. Neutron scattering on iridates is difficult to measure because of the strong absorption of neutrons by iridium, although some efforts to measure iridates using special experimental setups have been reported [47]. An important and complementary experimental route to probe the novel fractionalized excitations is provided by Raman spectroscopy. Importantly, Raman signatures contain, as we show below, two different but related signatures of the low-energy Majorana fermions: (1) the direct coupling of Majorana fermions to photons leading to a broad magnetic continuum [48–50] and (2) the additional decay of Raman-active phonons through their coupling to Majorana excitations via spin-phonon coupling. Positive identification of Majorana signatures in both of these aspects, we show, strongly suggests the relevance of Kitaev QSL physics in Cu_2IrO_3 with low-energy Majorana fermions. Indeed, in Raman scattering for γ- and β-Li_2IrO_3 [28], α-$RuCl_3$ [50–52], and $H_3LiIr_2O_6$ [43], a broad magnetic continuum has been detected in the low-energy Raman profile. Even though γ- and β-Li_2IrO_3 and α-$RuCl_3$ have magnetically ordered ground states, the temperature evolution of the magnetic background is typified by dominant Fermi statistics and has been attributed to the fractionalized Majorana fermions [28,50–52].

II. EXPERIMENTAL METHODS

High-quality polycrystalline samples of Cu_2IrO_3 were prepared by a low-temperature topotactic reaction of Na_2IrO_3 with CuCl as reported previously [32]. Powder x-ray diffraction confirmed the expected crystal structure ($C2/c$ space group), and ac and dc susceptibility measurements down to 300 mK (Appendix A) confirmed the absence of spin freezing, which has been reported to contaminate the low-temperature magnetism for some Cu_2IrO_3 materials reported previously [31,34].

The unpolarized Raman spectra at room temperature were recorded in a backscattering geometry using a HORIBA LabRAM HR Evolution spectrometer equipped with a thermoelectric cooled charge-coupled device (CCD; HORIBA Jobin Yvon, Syncerity 1024 × 256). The low-temperature Raman measurements were performed from 6 to 295 K with a 532-nm DPSS laser illuminating the sample with less than ∼1.5 mW power. Temperature variation was performed with a closed-cycle He cryostat (Cryostation S50, Montana Instruments) with a temperature stability of approximately ±1 K. The cross-polarized Raman spectra were recorded using a HORIBA LabRAM HR Evolution spectrometer with an ultralow-frequency (ULF) setup to record the spectrum down to 10 cm^{-1}. The low-temperature Raman measurements on that setup were performed from 4 to 300 K using a continuous-flow liquid helium cryostat (MicrostatHe2, Oxford Instruments) with a temperature stability of approximately ±1 K.

III. EXPERIMENTAL RESULTS

Figure 1 shows unpolarized and cross-polarized (to avoid any contribution from Rayleigh scattering at low frequencies) Raman spectra of Cu_2IrO_3 at a few representative temperatures with sharp phonon modes and a quasielastic scattering (QES) component (linewidth $\sim$50 cm^{-1}) superimposed on a broad continuum extending up to $\sim$600 cm^{-1}. As observed experimentally in the Kitaev materials α-$RuCl_3$ [50–52] and γ- and β-Li_2IrO_3 [28], phonons are superimposed on a broad background which is temperature dependent. This broad Raman background in experiments has been attributed to the gapless itinerant Majorana fermions of a Kitaev QSL. Finite-temperature simulations for the pure Kitaev model by Nasu *et al.* [49] reproduce the broad continuum with a band edge extending up to $\simeq 3|J_K|$ (arising from the Majorana fermion bandwidth), where J_K is the Kitaev coupling strength. As shown in Fig. 1, the upper cutoff of the magnetic continuum in Cu_2IrO_3 gives an experimental estimate for $|J_K| \approx 24$ meV, in good agreement with recent estimates (17–30 meV) from the low-energy spin excitation gap seen in NQR studies [34]. This intriguing broad magnetic continuum (Fig. 1) then begs for a careful closer investigation—a topic on which we shall now focus. This will be followed by a discussion of the low-energy quasielastic signal, whose weight appears to generically diminish at low temperature (see below).

A. Anomalies in frequencies and linewidths of Raman-active phonons

To further probe the signatures consistent with fractionalization of the spins into Majorana fermions, we now look for the effect of Majorana excitations on phonons, if any, especially at low temperatures ($T \lesssim J_K$). Such an effect should be particularly strong for the phonons embedded in or close to the magnetic continuum.

Of the 39 active Raman modes expected for monoclinic ($C2/c$) Cu_2IrO_3 ($\Gamma_{\text{Raman}} = 18A_g + 21B_g$), 13 modes could be detected at $\sim$6 K in the frequency range 70–800 cm^{-1} (8.7–99.2 meV). All the phonon modes except M2 are fitted with a symmetric Lorentzian profile function for the entire range of temperature. The M2 mode is fitted well with the asymmetric Breit-Wigner-Fano (BWF) line shape [Fig. 2(a)] arising from the interaction of the phonon with the magnetic continuum. The BWF line shape is given by [53]

$$I_{\text{BWF}}(\omega) = I_0 \frac{[1 + (\omega - \omega_0)/qw]^2}{1 + [(\omega - \omega_0)/w]^2}, \quad (1)$$

where ω, ω_0, $1/|q|$, w, and I_0 are the Raman shift, the spectral peak center, the asymmetry parameter, the spectral width, and the maximum intensity of the BWF line, respectively. The temperature dependence of the asymmetry parameter $1/|q|$ for the M2 mode is depicted in Fig. 2(b). The similar local symmetry of the edge-sharing octahedra in related Kitaev compounds α-$RuCl_3$ [54] and α-Li_2IrO_3 [55] allows us to qualitatively categorize the observed Raman modes in Cu_2IrO_3. While the low-frequency modes (M1, M2) correspond mainly to the relative motion of the in-plane Ir atoms, the high-frequency bands (M3, M4) are related to the IrO_6 octahedral vibrations including the breathing of the Ir-O-Ir-O ring, Ir-O-Ir-O plane shearing, and breathing of upper and lower oxygen layers. The overall phonon spectrum remains almost unchanged with increasing temperature except for the thermal broadening of weaker modes making them undetectable at higher temperatures. No change in the number of Raman modes confirms the stability of the ambient crystal symmetry down to 6 K. This is an advantage that Cu_2IrO_3 has over α-$RuCl_3$, which undergoes a structural transition around 140 K, further obscuring attempts to establish connections between the onset of Majorana fermions and phonons [52].

Normally, a monotonic temperature dependence of phonon parameters is expected because the phonon self-energies are typically determined by lattice anharmonicity which reduces monotonically with temperature [56]. This is, however, not the case in Cu_2IrO_3 with anomalous temperature evolution of frequencies and FWHMs of the phonon modes below $T \simeq$ 120 K. The temperature dependence of the frequency and FWHMs of the strong phonon modes (marked M1, M2, M3, and M4 in Figs. 1 and 10) is shown in Figs. 2(c) and 2(d). The solid blue curves are the fits from 295 to 120 K to the simple cubic anharmonic model [57] representing phonon (frequency ω) decay in two phonons of equal frequency ($\omega/2$) (see Appendix E for fitting details). The dashed curves are extrapolations of the fits to lower temperatures. The frequencies (FWHM) are lower (higher) than expected from the cubic anharmonic temperature dependence of phonons. The latter, in particular, is suggestive of extra channels provided by the magnetic continuum for the Raman-active phonons to decay. While this effect is most dramatic for M1 and M2 below $T \lesssim 120$ K $\approx 0.43\ J_K$, the M3 and M4 modes are not affected to much extent. The above anomaly is very much different from the phonon softening in magnetically ordered materials, such as Fe_3GeTe_2 [58], where similar anomalies are associated with the magnetic order. For Cu_2IrO_3, however, no such magnetic order is present down to the lowest temperature measured. Also, the strength of the Fano asymmetry, i.e., the value of $1/|q|$, depends on (1) the magnitude of the Loudon-Fleury vertex between the photon and the Majorana and (2) the magnetoelastic coupling strength. Hence the magnitude of the Fano asymmetry is expected to depend on the aforementioned coupling constants, and the enhancement of the $1/|q|$ parameter of the M2 mode below the Majorana crossover temperature T_h hints towards the coupling between the phonons and the fractionalized Majorana excitations as found in other candidate materials [28,52]. At this point we note that an estimated small fraction ($\approx$5%) of random singlets emerging below $\sim$20 K (see Appendix A) is incongruous to induce any anomaly in the phonon modes at the much higher temperature scale of 120 K.

Remarkably, the numerical studies [49,59] of the pure Kitaev model found that such a temperature scale, $T_h \sim$ 0.4–0.5 J_K, is associated with the completion of transfer of spectral weight of a coherent itinerant Majorana fermion to an incoherent one. Indeed, the above temperature is associated with the van Hove singularity of the free Majorana dispersion in the zero-flux sector whose depletion is completed at $T \sim T_h$. The above agreement of T_h of the pure Kitaev model numerics is seen for all the Raman-active modes. At this point, we note that for the Kitaev QSL there is another energy scale, $T_l \sim$ 0.012–0.015 J_K, associated with the Z_2 fluxes [19,49,59].

Although such low temperature is not accessible to the current experiment, the frequency (FWHM) of the phonon decreases (increases) monotonically till the lowest accessible temperature, $T \sim 6$ K.

B. Intensity of the M3 mode

In the absence of spin-lattice coupling, the temperature dependence of integrated intensities of Raman phonons should follow the conventional Bose-Einstein distribution. The high-frequency M3 mode ($\hbar\omega_{M3} \approx 63$ meV) shows a strong departure from the above expectation and shows a strong enhancement of intensity with decreasing temperatures as seen in Fig. 1. In fact, we find (see Appendix F) that the intensity of M3 closely follows the temperature dependence of the dc susceptibility and thus is dependent on the spin-spin correlation. The susceptibility, in turn, shows clear deviation from the high-temperature Curie-Weiss (CW) behavior below ~120 K. Such anomalous behavior can arise from transfer of magnetic dipole spectral weight to the phonons via spin-lattice coupling [60]. Indeed, the phonon intensities are expected to depend on the spin-spin correlations [61]. This reiterates the presence of sizable spin-lattice coupling in Cu_2IrO_3.

C. Low-energy magnetic continuum

Within the Kitaev QSL phenomenology, which presently forms the natural framework to understand the anomalous Raman scattering, we attribute the low-energy magnetic continuum to that of the Majorana fermions scattering from the Z_2 fluxes. In this regard, as shown in Ref. [49], the primary contribution to the magnetic continuum arises from the itinerant Majorana fermions interacting with the Raman photon, while the effect of the low-energy Z_2 fluxes on the Majorana fermions inside the QSL is to renormalize the fermion bandwidth and density of states [49,59]. As discussed in Ref. [49], there are two distinct contributions dominating over distinct energy scales. While at high energies the two-fermion creation processes dominate, at low energies simultaneous creation and annihilation of two fermions contribute substantial weight to the (integrated) Raman intensity.

We particularly focus on the former intermediate- to high-energy contribution, the details of which (see below) are relatively more robust than the low-energy signatures as discussed below. To this end, following Ref. [49], in order to extract the Majorana fermion energy scale from the low-energy continuum, following Ref. [49], the Raman intensity $I(\omega)$ is integrated over the intermediate frequency range of $\omega_{\min} < \omega < \omega_{\max}$ to obtain $I_{\rm mid} = \int_{\omega_{\min}}^{\omega_{\max}} I(\omega) d\omega$. The temperature dependence of $I_{\rm mid}$ in the frequency interval 120–260 $\rm cm^{-1}$ is plotted in Fig. 3(b). As is clear from Fig. 3(b), $I_{\rm mid}$ has a nonmonotonic temperature dependence with the high-temperature regime dominated by the standard one-particle scattering due to the thermal Bose factor $[1 + n(\omega_b)] = 1/(1 - e^{-\hbar\omega_b/k_BT})$, with $\omega_b = 11$ meV, extracted from the bosonic fit as a fitting parameter. This bosonic background is attributed to phonons since the system does not entertain other bosonic excitations such as magnons due to the lack of long-range spin ordering down to the lowest measurable temperature. A confirmation of this is obtained from the fact that the value of ω_b matches well with the strongest phonon mode at ~92 $\rm cm^{-1}$ in the low-frequency regime.

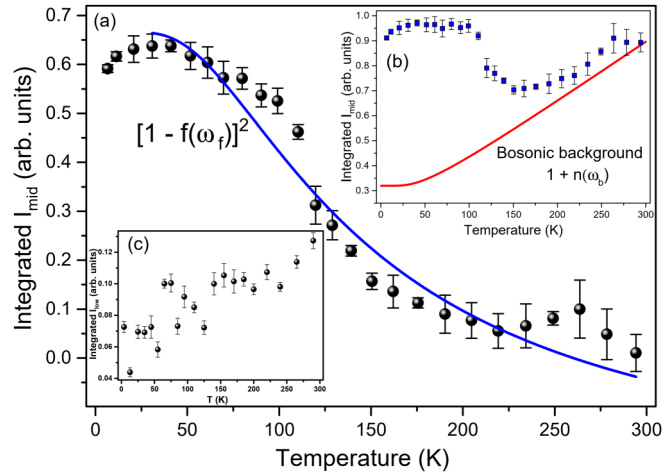

FIG. 3. (a) Symbols denote the magnetic contribution to integrated $I_{\rm mid}$ in the frequency range 120–260 $\rm cm^{-1}$ after subtracting the bosonic background [shown in (b)]. The blue solid curve represents fitting by the two-fermion scattering form $A + B(1 - f)^2$, with $f = 1/(1 + e^{\hbar\omega/k_BT})$ being the Fermi distribution function. (c) Symbols denote the magnetic continuum integrated in the low-frequency region of 10–45 $\rm cm^{-1}$.

Figure 3(a) demonstrates the temperature evolution of integrated $I_{\rm mid}$ after subtracting the nonmagnetic bosonic background. The magnetic contribution to $I_{\rm mid}$ is enhanced significantly below 120 K as clearly indicated by the deviation from thermal behavior and can be well fitted to the form [49] $A + B[1 - f(\omega_f)]^2$ with $\omega_f = 19$ meV, where $f(\omega_f) = 1/(1 + e^{\hbar\omega_f/k_BT})$ is the Fermi distribution function. This typical scaling of $I_{\rm mid}$, as mentioned above, is associated with the scattering contribution from the process of creation or annihilation of Majorana fermion pairs [49]. The Majorana energy scale for Cu_2IrO_3 is deduced from the fermionic fit with $\omega_f = 19$ meV ($\approx 0.8|J_K|$) and is in accordance with a Kitaev QSL phase considering similar energy scales gleaned for other Kitaev candidates [28,49].

A similar integrated intensity, $I_{\rm low}$, may be obtained on integration over a window $0 < \omega < \omega_{\min}$, which leads to a scaling of $f(1 - f)$ [49] at low temperatures and is sensitive to the low-energy fermion density of states. In Fig. 3(c) we plot $I_{\rm low}$ in the low-frequency interval of 10–45 $\rm cm^{-1}$ as obtained from the raw data in a cross-polarized setup, and it reveals a general decrease with decreasing temperature. While this is very encouragingly in qualitative agreement with the proposed scaling for the pure Kitaev model [49], our present experimental resolution does not allow us to make a quantitative comparison mainly due to the low photon count in the cross-polarized setup used for this experiment. The quantitative analysis of $I_{\rm low}$ is further complicated by the finite low-frequency quasielastic signal which owes its origin to the dilute disorder present in Cu_2IrO_3 in addition to small non-Kitaev interactions. Indeed, recent numerical calculations [45,62–64] show that nonmagnetic dilution of the honeycomb lattice for the pure Kitaev model can produce a large number of low-energy fermionic modes without

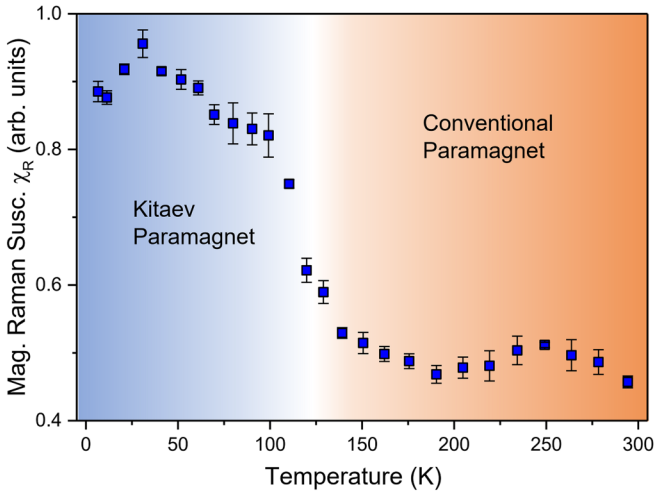

FIG. 4. Magnetic Raman susceptibility (Mag. Raman Susc.) as a function of temperature deduced from the Kramers-Kronig relation. The shaded regions mark the boundary between the conventional and Kitaev paramagnetic states.

destroying the essence of the Kitaev QSL. The interaction and the fate of these modes that are clearly relevant for Cu_2IrO_3 and their contribution to the low-energy density of states presently mask the pristine behavior of the low-energy Majorana fermions. However, the lack of magnetic order and the anomalous spin-phonon coupling (see below) along with the intermediate-energy fermionic magnetic continuum clearly show that the pure Kitaev model and Majorana fermions are the right starting point to understand the interplay of fractionalization and disorder at lower energies along with possible non-Kitaev interactions.

To further extract the Majorana essence from the magnetic background, the dynamic spin susceptibility χ_R is measured. The magnetic Raman susceptibility χ_R is extracted by integrating Raman conductivity $\frac{\chi''(\omega)}{\omega}$ in the frequency range 70–600 cm^{-1} using the Kramers-Kronig relation, $\chi_R = \lim_{\omega\to 0}\chi(k=0,\omega) \equiv \frac{2}{\pi}\int \frac{\chi''(\omega)}{\omega}d\omega$. The dynamical Raman tensor susceptibility $\chi''(\omega)$ is proportional to the Raman intensity as $I(\omega) = 2\pi\int\langle R(t)R(0)\rangle e^{i\omega t}dt \propto [1+n(\omega)]\chi''(\omega)$, where $R(t)$ is the Raman operator. Figure 4 displays the temperature dependence of χ_R, which shows that χ_R remains almost constant down to 120 K, below which it increases rapidly with decreasing temperature. In the Kitaev QSL state, the Raman operator couples to the dispersing Majorana fermions and extensively projects to the two-Majorana-fermion density of states (DOS) [48]. Thus an enhancement of χ_R below 120 K corresponds to significant enhancement of the Majorana DOS in the system driving the system from a simple paramagnet to a Kitaev paramagnet, also clearly reflected in the temperature dependence of $I_{\rm mid}$.

Both $I_{\rm mid}$ in Fig. 3 and χ_R in Fig. 4 show a subtle decrease below ∼25 K. At first glance, one may correlate this with the partial spin freezing reported for Cu_2IrO_3 below ∼10 K in recent μSR and NQR studies [33,34]. However, this may not be the case as our samples do not show evidence of spin freezing down to 2 K in ac χ (Appendix A) as well as down to 260 mK in μSR measurements [32]. It is tempting to associate the decrease in $I_{\rm mid}$ below 25 K (∼0.09 J_K) with the calculated $I_{\rm mid}$ determined by quantum Monte Carlo calculations (peaking at ∼0.07 J_K) [49].

IV. MAJORANA-PHONON COUPLING

In the absence of any thermal phase transition to a magnetic ordered state, the anomalous renormalization of the phonon frequency and increment in the linewidth at low temperatures suggest that new decay channels are opening up for the phonons to interact and possibly decay into. Given the current understanding of the phenomenology of Cu_2IrO_3 [32–34] and the encouraging match of the the energy scale T_h, it is natural to seek an explanation of the above experimental results in terms of the excitations of the Kitaev QSL, i.e., the Majorana fermions and Z_2 fluxes that result from the spin-(optical-)phonon coupling. Already, the existing calculations [49,59] correctly account for the broad magnetic background in Fig. 1 to this end.

We now show that the spin-phonon coupling leads to the possibility of a Yukawa-like coupling between a Majorana bilinear and the phonon somewhat akin to the electron-phonon coupling in superconductivity. This coupling, in turn, accounts for the experimental findings and hence provides a very interesting understanding of the experimental data in terms of the Majorana-phonon coupling. Below, we outline our calculations capturing the essence of the above physics. The Kitaev spin model is given by [19]

$$H_{\rm Kitaev} = \sum_{i,\alpha} J_{i,\alpha} S_i^\alpha S_{i+\hat{\alpha}}^\alpha, \tag{2}$$

where α denotes x, y, or z types of bonds and $\hat{\alpha}$ denotes the three nearest-neighbor vectors of the honeycomb lattice (see Fig. 12). The exchange couplings are functions of the ionic positions as they come from the overlap of the electronic wave functions. Thus, in the presence of lattice vibrations, we have [65]

$$J_{i,\alpha} = J_K + \frac{\partial J_{i,\alpha}}{\partial R^a_{i,\alpha}}\delta^a_{i,\alpha} + \frac{1}{2}\frac{\partial^2 J_{i,\alpha}}{\partial R^a_{i,\alpha}\partial R^b_{i,\alpha}}\delta^a_{i,\alpha}\delta^b_{i,\alpha}, \tag{3}$$

where the expansion is done about the equilibrium ionic positions of the crystal, $\bar{R}^a_{i,\alpha} = r^a_i - r^a_{i+\hat{\alpha}}$, with $\delta^a_{i,\alpha} = R^a_{i,\alpha} - \bar{R}^a_{i,\alpha}$ $(a = x, y)$ denoting the deformation of the bond, and the derivatives are evaluated at the equilibrium position $\bar{R}_{ij}$.

This leads to the spin-phonon Hamiltonian that dictates the coupled dynamics of the optical phonons and the spins

$$H = H_{\rm spin} + H_{\rm spin\text{-}phonon} + H_{\rm phonon}, \tag{4}$$

where $H_{\rm spin}$ is the bare spin Kitaev Hamiltonian of Eq. (2) with $J_{i,\alpha} \to J_K$, $H_{\rm phonon}$ is the bare harmonic phonon Hamiltonian, and

$$H_{\rm spin\text{-}phonon} = H_1 + H_2 \tag{5}$$

represents the spin-phonon coupling. The two terms denote the first- and second-order contributions of Eq. (3) and are given by

$$H_1 = \sum_{i,\alpha}\frac{\partial J_{i,\alpha}}{\partial R^a_{i,\alpha}}\delta^a_{i,\alpha}\, S_i^\alpha S_{i+\hat{\alpha}}^\alpha \tag{6}$$

and

$$H_2 = \frac{1}{2}\sum_{i,\alpha}\frac{\partial^2 J_{i,\alpha}}{\partial R^a_{i,\alpha}\partial R^b_{i,\alpha}}\delta^a_{i,\alpha}\delta^b_{i,\alpha}\, S_i^\alpha S_{i+\hat{\alpha}}^\alpha, \tag{7}$$

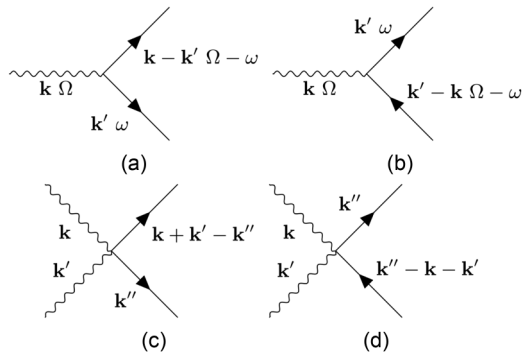

FIG. 5. (a) and (b) [(c) and (d)] denote the interaction between the phonon and matter fermion [66] coming from the first-order (second-order) contributions to the spin-phonon coupling.

respectively. Expressing the phonons in terms of their normal modes and neglecting the various form factors, which we expect to be unimportant for the generic temperature dependence that we are focusing on, we now obtain the renormalization of the phonon frequency and linewidth by calculating the self-energy correction to the phonon propagators due to the above spin-phonon interactions within a single-mode approximation for the phonons.

Within the Kitaev QSL phenomenology, we perform the standard Majorana decoupling of the spins to obtain (in the zero-flux sector) the scattering vertices between the matter fermions and the phonons as shown in Fig. 5. Here, we have performed the well-known [66] transformation of the Majoranas to the bond matter fermions for the Kitaev QSL. Also, Figs. 5(a) and 5(b) denote the interaction vertices arising due to H_1 [Eq. (6)], and Figs. 5(c) and 5(d) denote those arising due to H_2 [Eq. (7)].

These interactions clearly show that the phonon can decay into the fractionalized excitations of the QSL and this would renormalize both the frequency and the linewidth of the phonon peak. In regard to the linewidth, we expect an anomalous broadening as the temperature is decreased since on lowering the temperature the fermions become more coherent and hence the phonon can more efficiently decay into them while obeying all the conservation laws.

A. Frequency renormalization

The leading-order contribution to the renormalization of the frequency comes from Figs. 5(c) and 5(d) when we integrate over the fermions. From Eq. (7), the resultant frequency renormalization is given by

$$\delta\omega \propto \frac{1}{N_b}\sum_{i,\alpha}\langle \bar{J}_K\ S_i^{\alpha} S_{i+\hat{\alpha}}^{\alpha}\rangle_S, \tag{8}$$

where $\langle\cdots\rangle_S$ denotes averaging of the equal-time spin correlators over the thermodynamic ensemble and the proportionality constant is given in terms of the first-order spin-phonon coupling and the transformation to the phonon soft modes. For the present discussion we neglect their detailed structure and assume it to be a constant, λ.

Within a free-Majorana phenomenology, the spin energy can be calculated in the zero-flux sector to obtain an estimate of $\delta\omega$. This calculation is detailed in Appendix I, and it readily matches the expectation that the spin energy goes to zero at $T \to \infty$ and gradually turns nonzero around $T \sim J_K$ ultimately saturating to a negative constant number at zero temperature corresponding to the ground-state energy density of the spins (see Fig. 13). Furthermore, numerical calculations exist for finite temperatures including all the flux sectors for the pure Kitaev model [59] which show a rather sharp crossover from zero to nonzero values. With the energy being generally negative, this nominally suggests softening of the phonon frequency. We, however, note that the mode dependence of the above contribution is entirely due to the matrix elements which we have neglected in this calculation. Further temperature dependence can come from the real part of the self-energy of the bubble (see Appendix I for details).

B. Phonon linewidth

The leading contribution to the linewidth, however, comes from the bubble contributions arising due to the two vertices in Figs. 5(c) and 5(d). At finite temperature and in the presence of spin interactions beyond the pure Kitaev model, clearly the fermion lines would be further renormalized by the fermions' scattering with the Z_2 fluxes, which, in turn, provide a finite lifetime to the fermions as well as renormalize their bandwidth [19]. For very low temperature and within the exactly solvable model, we neglect the scattering with the gapped Z_2 fluxes, and then we have free Majorana fermions, which seems to be justified on the basis of numerical calculations [49,59] which show that the qualitative features of the matter fermion density of states remain intact at finite temperatures almost all the way up to T_h. Within this free-Majorana phenomenology, we now calculate the leading-order contribution to the Raman linewidth computing the self-energy bubble diagram for a particular normal mode (see Appendix I for details). The imaginary part of the phonon self-energy correction at the leading order is then given by

$$\begin{aligned}\mathrm{Im}[\Sigma(\mathbf{q},\omega+i0^+)] &\propto \frac{J_K^2}{N_b}\sum_{\mathbf{k}}[1-n_F(\epsilon_{\mathbf{k}})-n_F(\epsilon_{\mathbf{k}+\mathbf{q}})] \\ &\quad\times[\delta(\omega+\epsilon_{\mathbf{k}}+\epsilon_{\mathbf{k}+\mathbf{q}})-\delta(\omega-\epsilon_{\mathbf{k}}-\epsilon_{\mathbf{k}+\mathbf{q}})],\end{aligned} \tag{9}$$

where, again, the proportionality constant depends on the magnetoelastic coupling and the normal-mode matrix elements, which have been assumed to be a constant (χ) for this calculation. Here, $n_F(\epsilon_{\mathbf{k}})$ denotes the fermion occupancy of the complex fermionic modes with dispersion $\epsilon_{\mathbf{k}}$ in the zero-flux sector. This contribution, as the delta function indicates, arises due to the decay of the phonon into two fermions. As $T \to \infty$, the Majorana fermions become incoherent, and hence the above contribution to linewidth goes to zero, while at low temperatures it reaches a finite value for the completely coherent Majorana fermions.

This effect is completely opposite to the usual temperature-related broadening due to anharmonic terms and arises due to the development of a coherent scattering channel for the phonons. Clearly, in the absence of any magnetic phase transition, such coherent particles—in the case of a Kitaev QSL Majorana fermions—indicate novel low-temperature physics

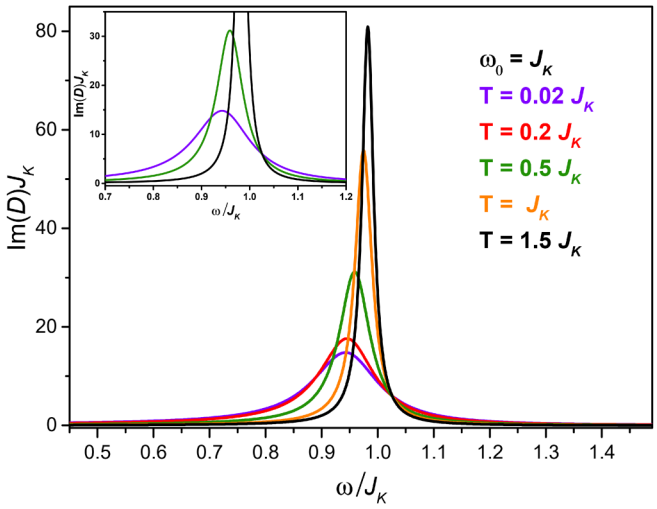

FIG. 6. Imaginary part of the phonon Green's function D with the frequency scaled with respect to the Kitaev coupling J_K. Different curves represent different temperatures. The spin-phonon coupling constants are taken as $\lambda = 0.13$ and $\chi = 0.2$.

in the spin sector. This is in direct conformity with the experimental observation. Once the flux excitation is taken into account, it only renormalizes the free-Majorana contribution without changing its qualitative features. We note that the real part of the self-energy coming from the bubble further renormalizes the phonon frequency and hence contributes to $\delta\omega$ in Eq. (8). Here, we neglect such higher-order contributions.

The phonon intensity obtained from the above calculation is given by the Lorentzian form

$$\frac{4\omega_0^2 \mathrm{Im}[\Sigma]}{\left(\omega^2 - \omega_0^2 - 2\omega_0\delta\omega\right)^2 + 4\omega_0^2 \mathrm{Im}[\Sigma]^2}, \tag{10}$$

where ω_0 is the bare phonon frequency of a particular normal mode. We evaluate the above expression considering the $q \to 0$ limit, which is relevant to the experiment [see Eq. (I8) of Appendix I].

We plot the Stokes line in Fig. 6. This is in qualitative agreement with the experimental data. A further comparison with the experimental data is obtained by fitting the results to the experimental data as shown in Appendix I.

To account for the temperature dependence of the intensity for the M3 mode, we note that the intensity is generically of the form [61] $|A + B_\alpha \langle S_i^\alpha S_{i+\hat{\alpha}}^\alpha \rangle|^2$, i.e., proportional to the nearest-neighbor spin correlations. This, within free Majorana fermions, can be calculated to yield a dependence proportional to $|\delta\omega|$ as is clear from Eq. (2). While such effects should appear for all the four modes, the particular sensitivity of M3 appears to us as a matrix-element effect that requires more detailed calculations.

V. SUMMARY AND OUTLOOK

To summarize, we have investigated the Raman response of the "second-generation" Kitaev QSL candidate Cu_2IrO_3. In addition to the the magnetic continuum (consistent with the Kitaev coupling, $J_K \approx 24$ meV) observed in the "first-generation" Kitaev materials, we observe clear anomalous renormalization of the Raman-active phonons below ~120 K. Encouraged by the conformity of the energy scales of the magnetic continuum and the phonon anomaly within a Kitaev phenomenology, we investigate the qualitative features of the Majorana-(optical-)phonon coupling to make an estimate for the phonon anomaly which accounts for the experimental observations.

Our results thus provide a strong indication for the relevance of Kitaev QSL physics and the immensely exciting possibility of positive identification of fractionalization in the nearly perfect honeycomb iridate Cu_2IrO_3. The phonon anomalies below a characteristic temperature provide yet another Raman signature of fractionalized Majorana fermions in addition to the magnetic continuum in prospective candidates of QSL. Although our samples have a smaller amount of Cu^{2+} impurities, as evidenced by the absence of a spin-glass transition or phase separation into QSL and magnetically frozen volume fractions [32], we do find that the residual ~5% Cu^{2+} impurities lead to a random-singlet phase below $T \sim$ 10–20 K. This small amount of disorder most likely also leads to the quasielastic Raman signal at low frequencies. This opens several interesting questions from both experimental and theoretical sides. On the experimental front, several future directions of study can be envisaged. Single crystals of Cu_2IrO_3 are not currently available. With high-quality single crystals, the intrinsic low-frequency Raman signal can be revealed and compared with expectations for the pure Kitaev model. Additionally, with single crystals, polarization-dependent Raman studies will become possible, which will allow a further quantitative comparison between theoretical calculations and experiments to further substantiate the physics of Majorana-phonon coupling. Furthermore, inelastic neutron scattering to measure the energy- and momentum-dependent excitation spectrum is desirable to be able to make quantitative comparisons with specific Hamiltonians including the Kitaev model and its extensions. Finally, crystals will allow looking for quantization in thermal Hall measurements, similar to what has been reported for α-$RuCl_3$ [20], although recent experimental works have shown that the field-induced paramagnetic state in $RuCl_3$ may not be a QSL after all [67,68]. On the theoretical side, the present calculations only take care of the free Majorana fermions while neglecting the fluxes as well as other non-Kitaev spin interactions. Their roles in the present calculations need to be quantitatively settled both for Cu_2IrO_3 and for other QSLs in general to investigate the physics of fractionalization through phonons.

Note added. Recently, other theoretical studies on spin-phonon coupling in a Kitaev QSL have been described in Refs. [69,70] which can further account for quantitative features of the vibrational Raman spectra in a Kitaev QSL beyond universal temperature dependence as attempted here. Such a quantitative treatment would require a more detailed knowledge of Hamiltonian and phonon parameters for Cu_2IrO_3 that is presently missing and forms an important future direction.

ACKNOWLEDGMENTS

A.K.S. thanks the Nanomission Council and the Year of Science professorship of DST for financial support.

P.S., A.A., and Y.S. thank the x-ray, liquid helium plant, and superconducting quantum interference device (SQUID) magnetometer facilities at IISER Mohali. S.B. acknowledges J. Knolle and R. Moessner for previous collaborations and A. Nanda and K. Damle for discussions. S.B. acknowledges the Max Planck Partner Grant at ICTS and SERB-DST (India), Project Grant No. ECR/2017/000504, for funding. S.B. and A.S. acknowledge the support of the Department of Atomic Energy, Government of India, under Project No. 12-R&D-TFR-5.10-1100.

APPENDIX A: MATERIALS AND MAGNETIC CHARACTERIZATION

High-quality polycrystalline samples of Cu_2IrO_3 were synthesized by an ion exchange reaction by mixing Na_2IrO_3 and CuCl in the mole ratio 1 : 2.05 [31]. The mixture with total mass 350 mg was pelletized, placed in an alumina crucible, and sealed under vacuum in a quartz tube. The tube was heated at 1 °C/min to 350 °C, kept at that temperature for 16 h, and then cooled to room temperature at the same rate. Then the product was ground into a fine powder and washed five times with ammonium hydroxide (NH_4OH) and twice with distilled water. After being washed, the resulting material was dried at room temperature under vacuum for 2 h.

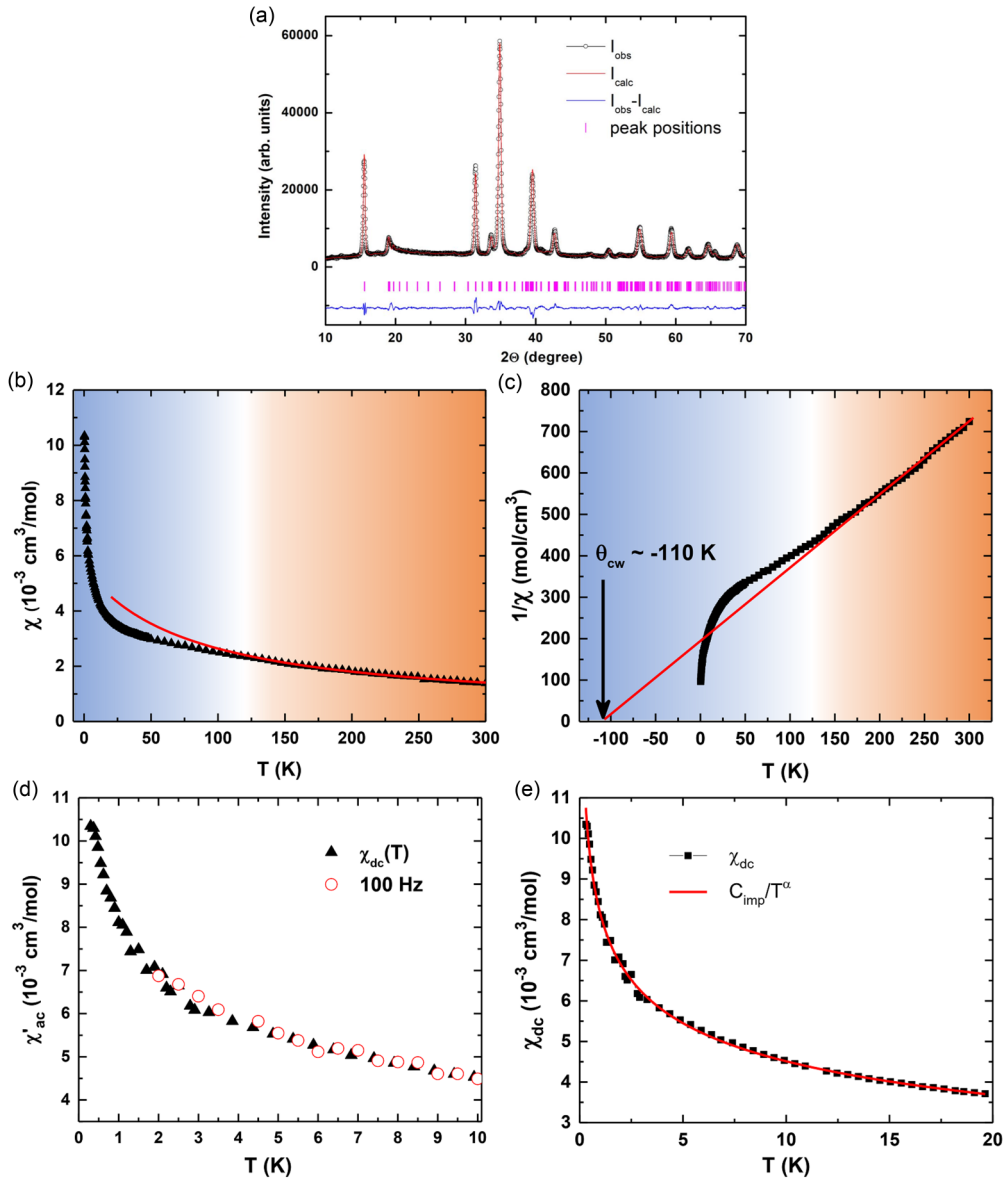

FIG. 7. (a) Powder x-ray diffraction pattern for Cu_2IrO_3 and its Rietveld refinement. (b) Temperature dependence of the dc magnetic susceptibility between 0.3 and 300 K. The red solid curve is the Curie-Weiss (CW) fit over the range 120–300 K. (c) Inverse susceptibility fitted to CW form (solid red line) over the range 120–300 K. The shaded regions demarcate the boundary between a conventional and Kitaev paramagnet where χ_{dc} starts deviating from the CW behavior. (d) Temperature variation of ac susceptibility down to 2 K in addition to the dc susceptibility down to 0.3 K. (e) Low-temperature χ_{dc} data fit to a sub-Curie law.

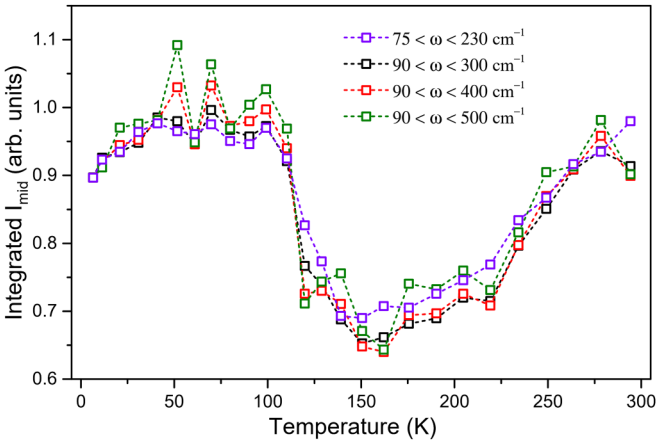

FIG. 8. Temperature dependence of integrated background intensity (normalized) for different energy ranges.

The powder x-ray diffraction pattern and a Rietveld refinement of the same are shown in Fig. 7(a) confirming that a single-phase product with the correct crystallographic structure (monoclinic $C2/c$) is obtained. The dc magnetic susceptibility between 0.3 and 300 K is shown in Fig. 7(b). The high-temperature χ in the region $120 < T < 300$ K is fit well with the Curie-Weiss (CW) form $\chi = \chi_0 + C/(T - \Theta_{CW})$ giving an effective moment close to $S = 1/2$ and $\Theta_{CW} \approx -100$ K. Figure 7(c) shows the CW behavior of the inverse dc susceptibility fitted in the range 120–300 K. The fit is extrapolated to extract the Curie-Weiss temperature $\Theta_{CW} \approx -110$ K. The deviation of susceptibility from the CW law below the Majorana crossover temperature T_h is similar to that observed in α-$RuCl_3$ [27] and in the quantum Monte Carlo calculations by Nasu *et al.* [59]. Below 10 K, the $1/\chi$ data show a sharp downturn, which is the contribution from disorder, the magnitude of which we estimate below. The χ_{dc} data below 10 K are shown in Fig. 7(d). We did not observe any signatures of spin-glass freezing reported previously [31]. The absence of freezing is confirmed by an ac susceptibility measurement down to 2 K, which is also shown in Fig. 7(d). Figure 7(e) shows that the low-temperature χ data follow a sub-Curie-law behavior $\chi = C_{imp}/T^{\alpha}$ with $C_{imp} \approx 0.019(3)$ cm^3 K mol^{-1} and $\alpha = 0.23(2)$. This T dependence is consistent with a random-singlet state. However, the magnitude of C_{imp} gives an ≈5% estimate for the fraction of impurity spins which participate in this low-temperature random-singlet state. This impurity concentration is roughly half of the previously reported samples for which a spin-glass state was observed in magnetic measurement [33].

APPENDIX B: CHOICE OF ω_{min} AND ω_{max} IN MIDFREQUENCY BACKGROUND

Theoretical predictions on the choice of ω_{min} and ω_{max} suggest the energy range of $0.5 < \omega/J < 1.25$ [49] which gives a frequency window of $97 < \omega < 242$ cm^{-1} for Cu_2IrO_3 taking $J_K = 24$ meV. However, still there is no strong foundation for selection of this intermediate energy range, and various scales have been chosen for different Kitaev materials. For instance, for Li_2IrO_3, I_{mid} was chosen to be $1.5 < \omega/J < 3$ [28], whereas for α-$RuCl_3$, an energy range of $0.6 < \omega/J < 1.9$ was adopted by the authors [52]. To inspect the robustness of the I_{mid} range selection for Cu_2IrO_3, we calculated the integrated areas of the background taking different ω ranges, and the results are plotted in Fig. 8. We find that the scaling behavior of I_{mid} is the same for these moderate variations of the window size. A range of $120 < \omega < 260$ cm^{-1} is chosen for Cu_2IrO_3 since it is least affected by the interference of strong phonon intensities.

APPENDIX C: DIFFERENT BOSONIC AND FERMIONIC FITS TO INTEGRATED I_{mid}

Figures 9(a) and 9(b) show the variation of the fermionic fit to the integrated intensity in the frequency range $120 < \omega < 260$ cm^{-1} taking small variations in the bosonic fits. The fitting parameter ω_f deviates in the first decimal place compared with the fit shown in Fig. 3, and hence the fermionic fit is robust under the modulations done in the bosonic background. The fitting in Fig. 3 is considered due to lower errors in the fitting parameters.

APPENDIX D: PHONON FITS

Figure 10 represents fitted Raman spectra at selected temperatures with the blue curves showing individual phonon modes.

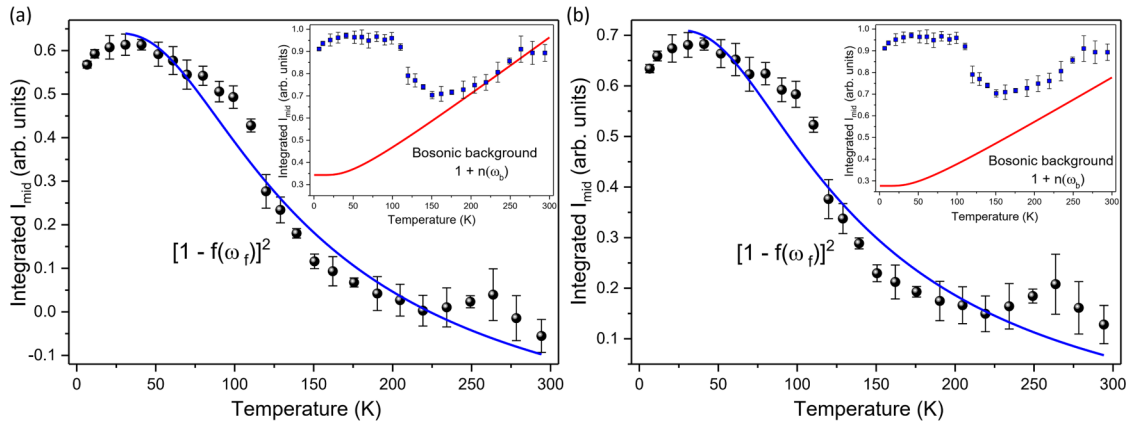

FIG. 9. (a) and (b) Fermionic fits to integrated I_{mid} with two different bosonic backgrounds (shown in the insets).

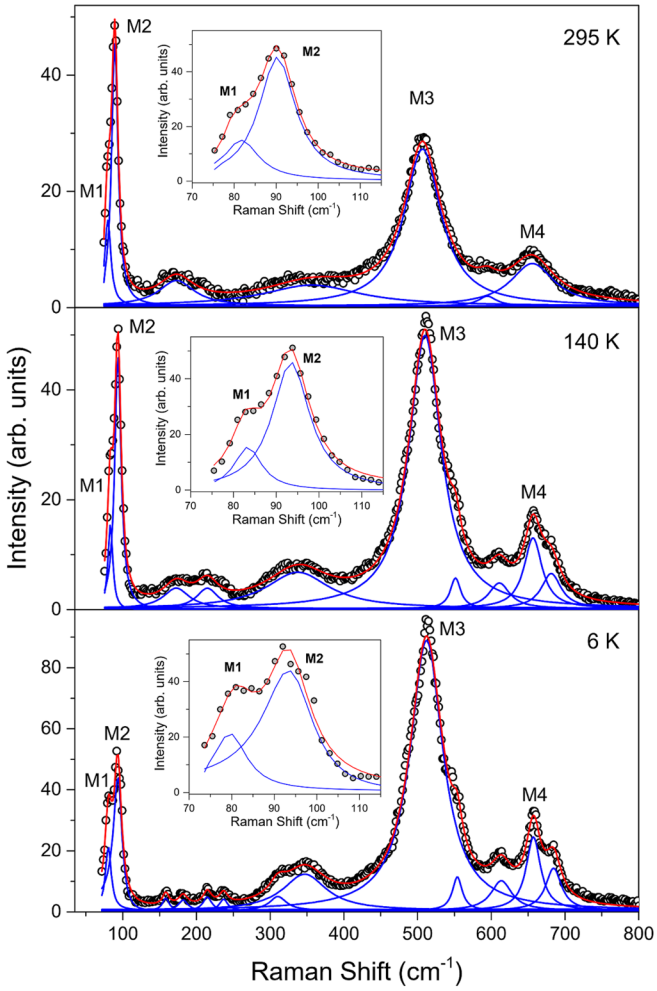

FIG. 10. Phonon fits (after subtracting the low-frequency background) to the Raman spectra of Cu_2IrO_3 at selected temperatures. Experimental data are indicated by black circles. Blue and red curves are individual phonon modes and the cumulative fits, respectively. The magnified M1-M2 doublets are shown in the insets.

APPENDIX E: LATTICE ANHARMONICITY

The impact of changing temperature on phonon population is well described under intrinsic anharmonic effects. Restricting to cubic corrections to phonon self-energy where a phonon decays into a pair of two phonons conserving energy and momenta, the phonon frequency and FWHM (real and imaginary parts of phonon self-energy, respectively) can be given as [57]

$$\omega(T) = \omega_0 + A\Big[1 + 2n\Big(\frac{\omega_0}{2}\Big)\Big], \tag{E1}$$

$$\Gamma(T) = \Gamma_0 + B\Big[1 + 2n\Big(\frac{\omega_0}{2}\Big)\Big], \tag{E2}$$

where ω_0 and Γ_0 are frequencies and linewidths at absolute zero, A (negative) and B (positive) are constants, and $n(\frac{\omega_0}{2})$ is the Bose-Einstein thermal factor. In the fits shown in the main text, ω_0 is extracted from the frequency fits in the high-temperature region (120–295 K) and those values of ω_0 are used to fit the FWHMs. The values for the fitting parameters ω_0, Γ_0, A, and B for different modes are shown in Table I.

TABLE I. List of fitting parameters for the cubic anharmonic fits to the phonon modes of Cu_2IrO_3.

Mode	ω_0	A	Γ_0	B
M1	84.1	−0.2	5.9	0
M2	95.5	−0.6	9.6	0
M3	518.1	−6.6	41.4	13.5
M4	659.9	−2.4	−58.3	86.54

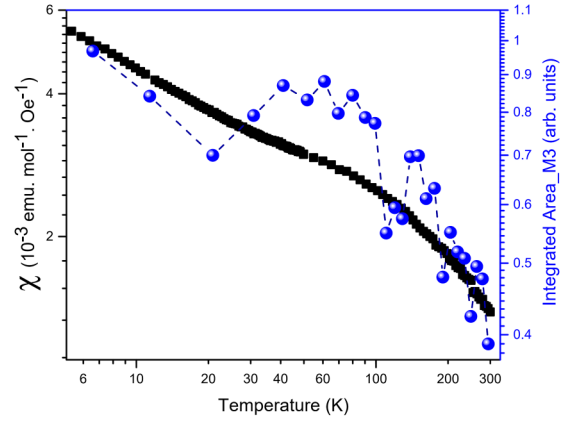

FIG. 11. Temperature variation of the integrated intensity of the M3 mode, similar to that of dc magnetic susceptibility, both plotted in log-log scale.

APPENDIX F: INTEGRATED INTENSITY OF HIGH-FREQUENCY M3 MODE

Figure 11 shows the temperature variation of integrated intensity of the 510 cm^{-1} Raman mode (M3) of Cu_2IrO_3 along with dc magnetic susceptibility. Both deviate from their high-temperature behavior below ∼120 K following modulation in the spin correlations in the Kitaev paramagnetic phase.

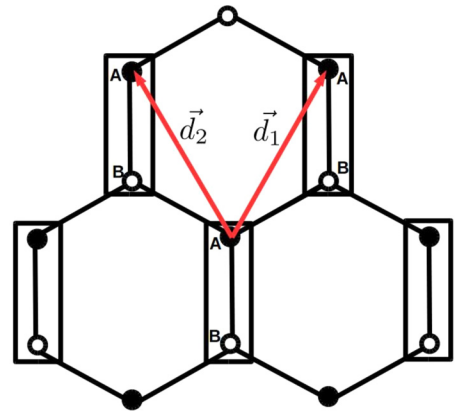

FIG. 12. The two-point unit cell has been considered along the z bonds. $\mathbf{d}_1$ and $\mathbf{d}_2$ denote the two lattice vectors of the honeycomb lattice.

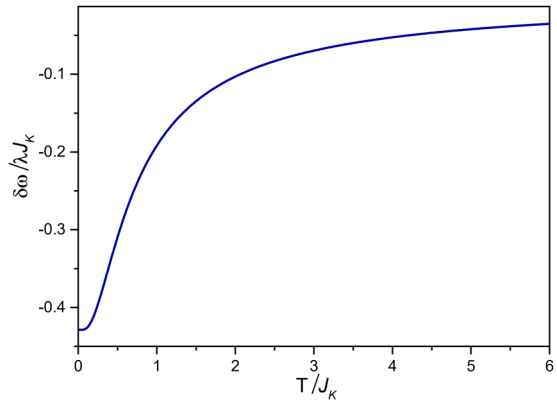

FIG. 13. Frequency shift is calculated from the average energy of the spin system. At zero temperature, the average energy saturates to approximately $-0.43\ J_K$.

APPENDIX G: DETAILS OF THE SPIN-PHONON COUPLING

1. Details of the phonon Hamiltonian and the single-mode approximation

The bare harmonic phonon Hamiltonian is given by

$$H_{\text{phonon}} = \sum_{i,\alpha} \frac{\mathbf{P}^2_{i,\alpha}}{2m} + \frac{1}{2}\sum_{i,\alpha} \mathcal{D}^{ab}_{\alpha\beta}\delta^a_{i,\alpha}\delta^b_{i,\beta}. \tag{G1}$$

We can go to the normal mode basis ($\mathbf{\Theta}_{i,\bar{p}}$) of phonons by a unitary rotation of $\boldsymbol{\delta}_{i,\alpha}$ which diagonalizes the matrix $\mathcal{D}^{ab}_{\alpha\beta}$.

$$\delta^a_{i,\alpha} = \Gamma^{ab}_{\alpha\bar{p}}\Theta^b_{i,\bar{p}}. \tag{G2}$$

In Appendixes G 2, H, and I, we will do a single-mode approximation and consider only a particular mode (say, $\bar{p}$) to calculate its frequency shift and linewidth broadening. With this assumption, we neglect the possible coupling between the normal modes through the spin-phonon interaction.

2. The spin-(optical-)phonon Hamiltonian

We rewrite the $H_{\text{spin-phonon}}$ [Eq. (5)] in terms of the normal modes.

$$H_1 = \sum_{i,\alpha} \frac{\partial J_{i,\alpha}}{\partial R^a_{i,\alpha}} \Gamma^{ab}_{\alpha\bar{p}}\Theta^b_{i,\bar{p}}\ S^\alpha_i S^\alpha_{i+\hat{\alpha}}, \tag{G3}$$

$$H_2 = \frac{1}{2}\sum_{i,\alpha} \frac{\partial^2 J_{i,\alpha}}{\partial R^a_{i,\alpha}\partial R^b_{i,\alpha}} \Gamma^{ac}_{\alpha\bar{p}}\Gamma^{bd}_{\alpha\bar{p}}\Theta^c_{i,\bar{p}}\Theta^d_{i,\bar{p}}\ S^\alpha_i S^\alpha_{i+\hat{\alpha}}. \tag{G4}$$

Here, the index $\bar{p}$ is not summed over. Usually, due to overlap of the orbitals, in insulators

$$J_{i,\alpha} = J_K e^{-\eta\delta_{i,\alpha}}, \tag{G5}$$

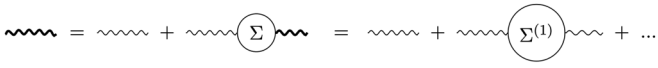

FIG. 14. The thick and thin curves denote the dressed and bare phonon Green's function, respectively. In the last diagram, we truncate the series up to the one-loop correction.

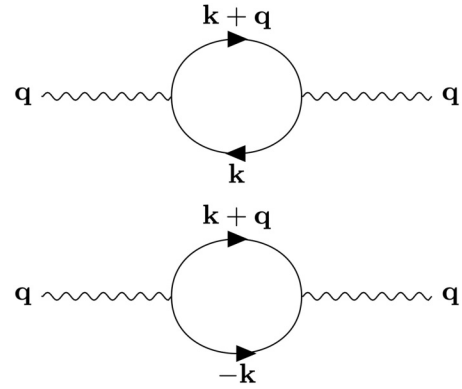

FIG. 15. The solid curves represent the propagator for "a" fermions.

where we have assumed a simplified isotropic form where η is the inverse length scale of decay of overlap. Using the above form, we further define the following notations for the compactness of the calculation:

$$\Gamma^{ab}_{\alpha\bar{p}}\frac{\partial}{\partial R^a_{i,\alpha}}e^{-\eta\delta_{i,\alpha}} \equiv \chi^b_{\bar{p},\alpha},$$

$$\frac{1}{2}\Gamma^{ac}_{\alpha\bar{p}}\Gamma^{bd}_{\alpha\bar{p}}\frac{\partial^2}{\partial R^a_{i,\alpha}\partial R^b_{i,\alpha}}e^{-\eta\delta_{i,\alpha}} \equiv \lambda^{cd}_{\bar{p},\alpha}. \tag{G6}$$

APPENDIX H: DETAILS OF THE MAJORANA-FERMION–(OPTICAL-) PHONON COUPLING

In this Appendix, we rewrite the $H_{\text{spin-phonon}}$ in terms of fractionalized Majorana degrees of freedom. We follow the standard Kitaev formulation [19] to write the spin as

$$S^\alpha_i = \frac{i}{2}b^\alpha_i c_i, \tag{H1}$$

where b^α_i and c_i are the four Majorana fermions. Therefore we have

$$S^\alpha_i S^\alpha_{i+\hat{\alpha}} = -\tfrac{1}{4}u^\alpha_{i,i+\hat{\alpha}}(ic_ic_{i+\hat{\alpha}}). \tag{H2}$$

Here, $u^\alpha_{i,i+\hat{\alpha}} = ib^\alpha_i b^\alpha_{i+\hat{\alpha}}$. The following calculations will be restricted to the zero-flux sector of the Z_2 connection, where we have $u^\alpha_{i,i+\hat{\alpha}} = +1$.

1. The linear term H_1

Using the above transformation, we write down Eq. (6) in terms of Majorana fermions.

$$H_1 = -\frac{J_K}{4}\sum_{i,\alpha}\chi^a_{\bar{p},\alpha}\Theta^a_{i,\bar{p}}(ic_ic_{i+\hat{\alpha}}). \tag{H3}$$

As mentioned in the main text, we now ignore all the matrix-element effects and assume $\chi^a_{\bar{p},\alpha} \equiv \chi^a$. This assumption only changes the vertex functions of the Feynman diagram. It does not really change the nature of the virtual processes involved which contribute to the self-energy of the phonon. For convenience of calculations, we convert the Majorana operators to complex fermion operators (bond matter fermion) within each unit cell (we take two sites joined by a z

bond as the unit cell; see Fig. 12) as [66]

$$c_i = \begin{cases} f_i + f_i^\dagger & \forall\, i \in A \\ i(f_i - f_i^\dagger) & \forall\, i \in B. \end{cases} \tag{H4}$$

Using this, we get

$$\begin{aligned} H_1 = \frac{J_K}{4} \sum_i \chi^a \Theta^a_{i,\bar{p}} \big[& (2 f_i^\dagger f_i - 1) \\ & + \left(f_i f_{i+\mathbf{d_1}} + f_i^\dagger f_{i+\mathbf{d_1}} - f_i f_{i+\mathbf{d_1}}^\dagger - f_i^\dagger f_{i+\mathbf{d_1}}^\dagger \right) \\ & + \left(f_i f_{i+\mathbf{d_2}} + f_i^\dagger f_{i+\mathbf{d_2}} - f_i f_{i+\mathbf{d_2}}^\dagger - f_i^\dagger f_{i+\mathbf{d_2}}^\dagger \right) \big]. \end{aligned} \tag{H5}$$

Using the following Fourier transformation,

$$f_i = \frac{1}{\sqrt{N_b}} \sum_{\mathbf{k}} e^{i\mathbf{k}\cdot\mathbf{r}_i} f_{\mathbf{k}}, \quad \Theta^a_{i,\bar{p}} = \frac{1}{\sqrt{N_b}} \sum_{\mathbf{k}} e^{i\mathbf{k}\cdot\mathbf{r}_i}\, \Theta^a_{\mathbf{k},\bar{p}}, \tag{H6}$$

the above Hamiltonian can be written as

$$\begin{aligned} H_1 = \frac{J_K}{4\sqrt{N_b}} \sum_{\mathbf{k},\mathbf{k}'} \chi^a \Theta^a_{\mathbf{k},\bar{p}} \big[& \mathcal{A}_{\mathbf{k},\mathbf{k}'} f^\dagger_{\mathbf{k}'} f_{\mathbf{k}'-\mathbf{k}} + \mathcal{B}_{\mathbf{k},\mathbf{k}'} f_{\mathbf{k}'} f_{-\mathbf{k}-\mathbf{k}'} \\ & + \mathcal{C}_{\mathbf{k},\mathbf{k}'} f_{\mathbf{k}'} f^\dagger_{\mathbf{k}+\mathbf{k}'} + \mathcal{D}_{\mathbf{k},\mathbf{k}'} f^\dagger_{\mathbf{k}'} f^\dagger_{\mathbf{k}-\mathbf{k}'} \big], \end{aligned} \tag{H7}$$

where

$$\begin{aligned} \mathcal{A}_{\mathbf{k},\mathbf{k}'} &= [2 + e^{i(\mathbf{k}'-\mathbf{k})\cdot\mathbf{d}_1} + e^{i(\mathbf{k}'-\mathbf{k})\cdot\mathbf{d}_2}], \\ \mathcal{B}_{\mathbf{k},\mathbf{k}'} &= [e^{-i(\mathbf{k}+\mathbf{k}')\cdot\mathbf{d}_1} + e^{-i(\mathbf{k}+\mathbf{k}')\cdot\mathbf{d}_2}], \\ \mathcal{C}_{\mathbf{k},\mathbf{k}'} &= [-e^{-i(\mathbf{k}+\mathbf{k}')\cdot\mathbf{d}_1} - e^{-i(\mathbf{k}+\mathbf{k}')\cdot\mathbf{d}_2}], \\ \mathcal{D}_{\mathbf{k},\mathbf{k}'} &= [-e^{i(\mathbf{k}'-\mathbf{k})\cdot\mathbf{d}_1} - e^{i(\mathbf{k}'-\mathbf{k})\cdot\mathbf{d}_2}]. \end{aligned} \tag{H8}$$

The Feynman diagrams for the above interaction are shown in Figs. 5(a) and 5(b). Now we use the following transformation, which is a standard Bogoliubov rotation, to diagonalize the free-Majorana Hamiltonian [66]:

$$\begin{bmatrix} f_{\mathbf{k}} \\ f^\dagger_{-\mathbf{k}} \end{bmatrix} = \begin{bmatrix} \cos\theta_{\mathbf{k}} & i\sin\theta_{\mathbf{k}} \\ i\sin\theta_{\mathbf{k}} & \cos\theta_{\mathbf{k}} \end{bmatrix} \begin{bmatrix} a_{\mathbf{k}} \\ a^\dagger_{-\mathbf{k}} \end{bmatrix}. \tag{H9}$$

Here, $\tan 2\theta_{\mathbf{k}} = -\frac{\mathrm{Im}S(\mathbf{k})}{\mathrm{Re}S(\mathbf{k})}$ and $S(\mathbf{k}) = \frac{J_K}{4}(1 + e^{i\mathbf{k}\cdot\mathbf{d}_1} + e^{i\mathbf{k}\cdot\mathbf{d}_2})$.

Using this transformation, we can rewrite Eq. (H7) in terms of these new fermions (a and $a^\dagger$), which are the normal modes of the zero-flux sector.

$$\begin{aligned} H_1 = \frac{J_K}{4\sqrt{N_b}} \sum_{\mathbf{k},\mathbf{k}'} \chi^a \Theta^a_{\mathbf{k},\bar{p}} \big[& \bar{\mathcal{A}}_{\mathbf{k},\mathbf{k}'}\; a_{-\mathbf{k}'} a_{\mathbf{k}'-\mathbf{k}} \\ & + \bar{\mathcal{B}}_{\mathbf{k},\mathbf{k}'}\; a_{-\mathbf{k}'} a^\dagger_{\mathbf{k}-\mathbf{k}'} + \bar{\mathcal{C}}_{\mathbf{k},\mathbf{k}'}\; a^\dagger_{\mathbf{k}'} a_{\mathbf{k}'-\mathbf{k}} + \bar{\mathcal{D}}_{\mathbf{k},\mathbf{k}'}\; a^\dagger_{\mathbf{k}'} a^\dagger_{\mathbf{k}-\mathbf{k}'} \big]. \end{aligned} \tag{H10}$$

Here, the vertex functions $\bar{\mathcal{A}}_{\mathbf{k},\mathbf{k}}$, $\bar{\mathcal{B}}_{\mathbf{k},\mathbf{k}'}$, $\bar{\mathcal{C}}_{\mathbf{k},\mathbf{k}'}$, and $\bar{\mathcal{D}}_{\mathbf{k},\mathbf{k}'}$ are given by

$$\begin{aligned} \bar{\mathcal{A}}_{\mathbf{k},\mathbf{k}'} &= i\sin\theta_{-\mathbf{k}'}\cos\theta_{\mathbf{k}'-\mathbf{k}}\mathcal{A}_{\mathbf{k},\mathbf{k}'} + \cos\theta_{-\mathbf{k}'}\cos\theta_{\mathbf{k}'-\mathbf{k}}\mathcal{B}_{\mathbf{k},-\mathbf{k}'} + i\cos\theta_{-\mathbf{k}'}\sin\theta_{\mathbf{k}'-\mathbf{k}}\mathcal{C}_{\mathbf{k},-\mathbf{k}'} - \sin\theta_{-\mathbf{k}'}\sin\theta_{\mathbf{k}'-\mathbf{k}}\mathcal{D}_{\mathbf{k},\mathbf{k}'}, \\ \bar{\mathcal{B}}_{\mathbf{k},\mathbf{k}'} &= -\sin\theta_{-\mathbf{k}'}\sin\theta_{\mathbf{k}'-\mathbf{k}}\mathcal{A}_{\mathbf{k},\mathbf{k}'} + i\cos\theta_{-\mathbf{k}'}\sin\theta_{\mathbf{k}'-\mathbf{k}}\mathcal{B}_{\mathbf{k},-\mathbf{k}'} + \cos\theta_{-\mathbf{k}'}\cos\theta_{\mathbf{k}'-\mathbf{k}}\mathcal{C}_{\mathbf{k},-\mathbf{k}'} + i\sin\theta_{-\mathbf{k}'}\cos\theta_{\mathbf{k}'-\mathbf{k}}\mathcal{D}_{\mathbf{k},\mathbf{k}'}, \\ \bar{\mathcal{C}}_{\mathbf{k},\mathbf{k}'} &= \cos\theta_{-\mathbf{k}'}\cos\theta_{\mathbf{k}'-\mathbf{k}}\mathcal{A}_{\mathbf{k},\mathbf{k}'} + i\sin\theta_{-\mathbf{k}'}\cos\theta_{\mathbf{k}'-\mathbf{k}}\mathcal{B}_{\mathbf{k},-\mathbf{k}'} - \sin\theta_{-\mathbf{k}'}\sin\theta_{\mathbf{k}'-\mathbf{k}}\mathcal{C}_{\mathbf{k},-\mathbf{k}'} + i\cos\theta_{-\mathbf{k}'}\sin\theta_{\mathbf{k}'-\mathbf{k}}\mathcal{D}_{\mathbf{k},\mathbf{k}'}, \\ \bar{\mathcal{D}}_{\mathbf{k},\mathbf{k}'} &= i\cos\theta_{-\mathbf{k}'}\sin\theta_{\mathbf{k}'-\mathbf{k}}\mathcal{A}_{\mathbf{k},\mathbf{k}'} - \sin\theta_{-\mathbf{k}'}\sin\theta_{\mathbf{k}'-\mathbf{k}}\mathcal{B}_{\mathbf{k},-\mathbf{k}'} + i\sin\theta_{-\mathbf{k}'}\cos\theta_{\mathbf{k}'-\mathbf{k}}\mathcal{C}_{\mathbf{k},-\mathbf{k}'} + \cos\theta_{-\mathbf{k}'}\cos\theta_{\mathbf{k}'-\mathbf{k}}\mathcal{D}_{\mathbf{k},\mathbf{k}'}. \end{aligned} \tag{H11}$$

2. The quadratic term H_2

In the zero-flux sector, H_2 can be written in terms of Majorana fermions in the following way:

$$H_2 = -\frac{J_K}{4} \sum_{i,\alpha} \lambda^{cd}_{\bar{p},\alpha}\; \Theta^c_{i,\bar{p}} \Theta^d_{i,\bar{p}}\; (i c_i c_{i+\hat{\alpha}}). \tag{H12}$$

Now we take an approximation similar to the case of linear coupling considering $\lambda^{cd}_{\bar{p},\alpha} = \lambda^{cd}$. Furthermore, transforming the Majorana fermions into complex fermions and going to the Fourier basis, we obtain (up to a bare phonon term)

$$H_2 = \frac{J_K}{4N_b} \sum_{\mathbf{k},\mathbf{k}',\mathbf{k}''} \lambda^{cd}\; \Theta^c_{\mathbf{k},\bar{p}} \Theta^d_{\mathbf{k}',\bar{p}} [\mathcal{P}_{\mathbf{k},\mathbf{k}',\mathbf{k}''} f^\dagger_{\mathbf{k}''} f_{\mathbf{k}''-\mathbf{k}-\mathbf{k}'} + \mathcal{Q}_{\mathbf{k},\mathbf{k}',\mathbf{k}''} f_{\mathbf{k}''} f_{-\mathbf{k}-\mathbf{k}'-\mathbf{k}''} + \mathcal{R}_{\mathbf{k},\mathbf{k}',\mathbf{k}''} f_{\mathbf{k}''} f^\dagger_{\mathbf{k}+\mathbf{k}'+\mathbf{k}''} + \mathcal{S}_{\mathbf{k},\mathbf{k}',\mathbf{k}''} f^\dagger_{\mathbf{k}''} f^\dagger_{\mathbf{k}+\mathbf{k}'-\mathbf{k}''}], \tag{H13}$$

where

$$\begin{aligned} \mathcal{P}_{\mathbf{k},\mathbf{k}',\mathbf{k}''} &= 2 + e^{i(\mathbf{k}''-\mathbf{k}-\mathbf{k}')\cdot\mathbf{d}_1} + e^{i(\mathbf{k}''-\mathbf{k}-\mathbf{k}')\cdot\mathbf{d}_2}, \quad \mathcal{Q}_{\mathbf{k},\mathbf{k}',\mathbf{k}''} = e^{-i(\mathbf{k}+\mathbf{k}'+\mathbf{k}'')\cdot\mathbf{d}_1} + e^{-i(\mathbf{k}+\mathbf{k}'+\mathbf{k}'')\cdot\mathbf{d}_2}, \\ \mathcal{R}_{\mathbf{k},\mathbf{k}',\mathbf{k}''} &= -e^{-i(\mathbf{k}+\mathbf{k}'+\mathbf{k}'')\cdot\mathbf{d}_1} - e^{-i(\mathbf{k}+\mathbf{k}'+\mathbf{k}'')\cdot\mathbf{d}_2}, \quad \mathcal{S}_{\mathbf{k},\mathbf{k}',\mathbf{k}''} = -e^{i(\mathbf{k}''-\mathbf{k}-\mathbf{k}')\cdot\mathbf{d}_1} - e^{i(\mathbf{k}''-\mathbf{k}-\mathbf{k}')\cdot\mathbf{d}_2}. \end{aligned} \tag{H14}$$

The Feynman diagrams for the above interaction are shown in Figs. 5(c) and 5(d). Now using Eq. (H9), we get

$$H_2 = \frac{J_K}{4N_b} \sum_{\mathbf{k},\mathbf{k}',\mathbf{k}''} \lambda^{cd}\; \Theta^c_{\mathbf{k},\bar{p}} \Theta^d_{\mathbf{k}',\bar{p}} [\bar{\mathcal{P}}_{\mathbf{k},\mathbf{k}',\mathbf{k}''} a_{-\mathbf{k}''} a_{\mathbf{k}''-\mathbf{k}-\mathbf{k}'} + \bar{\mathcal{Q}}_{\mathbf{k},\mathbf{k}',\mathbf{k}''} a_{-\mathbf{k}''} a^\dagger_{\mathbf{k}+\mathbf{k}'-\mathbf{k}''} + \bar{\mathcal{R}}_{\mathbf{k},\mathbf{k}',\mathbf{k}''} a^\dagger_{\mathbf{k}''} a_{\mathbf{k}''-\mathbf{k}-\mathbf{k}'} + \bar{\mathcal{S}}_{\mathbf{k},\mathbf{k}',\mathbf{k}''} a^\dagger_{\mathbf{k}''} a^\dagger_{\mathbf{k}+\mathbf{k}'-\mathbf{k}''}], \tag{H15}$$

where

$$\begin{aligned}
\bar{\mathcal{P}}_{\mathbf{k},\mathbf{k}',\mathbf{k}''} &= i\sin\theta_{-\mathbf{k}''}\cos\theta_{\mathbf{k}''-\mathbf{k}-\mathbf{k}'}\mathcal{P}_{\mathbf{k},\mathbf{k}',\mathbf{k}''} + \cos\theta_{-\mathbf{k}''}\cos\theta_{\mathbf{k}''-\mathbf{k}-\mathbf{k}'}\mathcal{Q}_{\mathbf{k},\mathbf{k}',-\mathbf{k}''} \\
&\quad + i\cos\theta_{-\mathbf{k}''}\sin\theta_{\mathbf{k}''-\mathbf{k}-\mathbf{k}'}\mathcal{R}_{\mathbf{k},\mathbf{k}',-\mathbf{k}''} - \sin\theta_{-\mathbf{k}''}\sin\theta_{\mathbf{k}''-\mathbf{k}-\mathbf{k}'}\mathcal{S}_{\mathbf{k},\mathbf{k}',\mathbf{k}''}, \\
\bar{\mathcal{Q}}_{\mathbf{k},\mathbf{k}',\mathbf{k}''} &= -\sin\theta_{-\mathbf{k}''}\sin\theta_{\mathbf{k}''-\mathbf{k}-\mathbf{k}'}\mathcal{P}_{\mathbf{k},\mathbf{k}',\mathbf{k}''} + i\cos\theta_{-\mathbf{k}''}\sin\theta_{\mathbf{k}''-\mathbf{k}-\mathbf{k}'}\mathcal{Q}_{\mathbf{k},\mathbf{k}',-\mathbf{k}''} \\
&\quad + \cos\theta_{-\mathbf{k}''}\cos\theta_{\mathbf{k}''-\mathbf{k}-\mathbf{k}'}\mathcal{R}_{\mathbf{k},\mathbf{k}',-\mathbf{k}''} + i\sin\theta_{-\mathbf{k}''}\cos\theta_{\mathbf{k}''-\mathbf{k}-\mathbf{k}'}\mathcal{S}_{\mathbf{k},\mathbf{k}',\mathbf{k}''}, \\
\bar{\mathcal{R}}_{\mathbf{k},\mathbf{k}',\mathbf{k}''} &= \cos\theta_{-\mathbf{k}''}\cos\theta_{\mathbf{k}''-\mathbf{k}-\mathbf{k}'}\mathcal{P}_{\mathbf{k},\mathbf{k}',\mathbf{k}''} + i\sin\theta_{-\mathbf{k}''}\cos\theta_{\mathbf{k}''-\mathbf{k}-\mathbf{k}'}\mathcal{Q}_{\mathbf{k},\mathbf{k}',-\mathbf{k}''} \\
&\quad - \sin\theta_{-\mathbf{k}''}\sin\theta_{\mathbf{k}''-\mathbf{k}-\mathbf{k}'}\mathcal{R}_{\mathbf{k},\mathbf{k}',-\mathbf{k}''} + i\cos\theta_{-\mathbf{k}''}\sin\theta_{\mathbf{k}''-\mathbf{k}-\mathbf{k}'}\mathcal{S}_{\mathbf{k},\mathbf{k}',\mathbf{k}''}, \\
\bar{\mathcal{S}}_{\mathbf{k},\mathbf{k}',\mathbf{k}''} &= i\cos\theta_{-\mathbf{k}''}\sin\theta_{\mathbf{k}''-\mathbf{k}-\mathbf{k}'}\mathcal{P}_{\mathbf{k},\mathbf{k}',\mathbf{k}''} - \sin\theta_{-\mathbf{k}''}\sin\theta_{\mathbf{k}''-\mathbf{k}-\mathbf{k}'}\mathcal{Q}_{\mathbf{k},\mathbf{k}',-\mathbf{k}''} \\
&\quad + i\sin\theta_{-\mathbf{k}''}\cos\theta_{\mathbf{k}''-\mathbf{k}-\mathbf{k}'}\mathcal{R}_{\mathbf{k},\mathbf{k}',-\mathbf{k}''} + \cos\theta_{-\mathbf{k}''}\cos\theta_{\mathbf{k}''-\mathbf{k}-\mathbf{k}'}\mathcal{S}_{\mathbf{k},\mathbf{k}',\mathbf{k}''}.
\end{aligned} \tag{H16}$$

APPENDIX I: THE RENORMALIZATION OF THE RAMAN-ACTIVE PHONONS

1. Frequency shift

In the low-temperature QSL regime of the experiment, the spin dynamics is expected to be slower than the optical phonons and hence to the first approximation, the spins can be approximated with their static equal-time configuration such that to the leading order, we obtain

$$H_{\text{spin-phonon}} \to \langle H_{\text{spin-phonon}}\rangle_S, \tag{I1}$$

where $\langle\hat{O}\rangle_S = \frac{\mathrm{Tr}(\hat{O}e^{-\beta H_{\text{spin}}})}{\mathrm{Tr}(e^{-\beta H_{\text{spin}}})}$ [H_{spin} is the bare spin Hamiltonian as mentioned in Eq. (4)] denotes averaging of the equal-time spin correlators over the thermodynamic ensemble. The spin correlators being time independent, they now act as a linear and quadratic deformation to H_{phonon}. Thus, within the harmonic phonon approximation valid for low temperatures, the linear term $\langle H_1\rangle_S$ does not affect the phonon frequency, which is entirely affected by $\langle H_2\rangle_S$ and is given by Eq. (8) of the main text. In the zero-flux approximation, it can be further calculated using free-Majorana phenomenology.

$$\delta\omega \sim \lambda J_K \sum_{\mathbf{k}} \left\langle \epsilon_{\mathbf{k}}\left(a^{\dagger}_{\mathbf{k}}a_{\mathbf{k}} - \frac{1}{2}\right)\right\rangle_S. \tag{I2}$$

Clearly, the above expression is directly proportional to the energy of the spin system and therefore always negative. This explains the softening of the phonon with decreasing temperature (see Fig. 13). Although the zero-flux approximation is not valid for the experimentally relevant temperature regime, the flux excitation only renormalizes the above contribution to the frequency.

2. Linewidth of phonon

The linewidth of the phonon peak is obtained by computing the phonon self-energy Σ defined by the Dyson equation

$$D = D_0 + D_0\Sigma D, \tag{I3}$$

where D_0 and D are the bare and dressed propagator of the phonon, respectively, as given in the main text. The above equation is diagrammatically represented in Fig. 14.

This series can be computed perturbatively under the assumption that spin-phonon coupling is the weakest energy scale of the problem. Here, we go up to the one-loop contribution. At this order, the self-energy can be computed from the Feynman diagrams shown in Fig. 15.

$$\begin{aligned}
\Sigma(\mathbf{q}, i\omega) &\sim -\frac{\chi^2 J_K^2}{N_b\beta}\sum_{\omega_m,\mathbf{k}}[M_{\mathbf{k}+\mathbf{q},\mathbf{k}}G(\mathbf{k}+\mathbf{q}, -i\omega - i\omega_m)G(-\mathbf{k}, i\omega_m) + M_{-\mathbf{k}-\mathbf{q},-\mathbf{k}}G(\mathbf{k}+\mathbf{q}, i\omega - i\omega_m)G(-\mathbf{k}, i\omega_m) \\
&\quad + N_{\mathbf{k}+\mathbf{q},\mathbf{k}}G(\mathbf{k}+\mathbf{q}, i\omega + i\omega_m)G(\mathbf{k}, i\omega_m) + N_{-\mathbf{k}-\mathbf{q},-\mathbf{k}}G(\mathbf{k}+\mathbf{q}, -i\omega + i\omega_m)G(\mathbf{k}, i\omega_m)] \\
&= \frac{\chi^2 J_K^2}{N_b\beta}\sum_{\mathbf{k}}\sum_{\omega_m}\left[M_{\mathbf{k}+\mathbf{q},\mathbf{k}}\frac{1}{i\omega + i\omega_m + \epsilon_{\mathbf{k}+\mathbf{q}}}\frac{1}{i\omega_m - \epsilon_{\mathbf{k}}} - M_{-\mathbf{k}-\mathbf{q},-\mathbf{k}}\frac{1}{i\omega - i\omega_m - \epsilon_{\mathbf{k}+\mathbf{q}}}\frac{1}{i\omega_m - \epsilon_{\mathbf{k}}}\right. \\
&\quad \left. - N_{\mathbf{k}+\mathbf{q},\mathbf{k}}\frac{1}{i\omega + i\omega_m - \epsilon_{\mathbf{k}+\mathbf{q}}}\frac{1}{i\omega_m - \epsilon_{\mathbf{k}}} + N_{-\mathbf{k}-\mathbf{q},-\mathbf{k}}\frac{1}{i\omega - i\omega_m + \epsilon_{\mathbf{k}+\mathbf{q}}}\frac{1}{i\omega_m - \epsilon_{\mathbf{k}}}\right],
\end{aligned} \tag{I4}$$

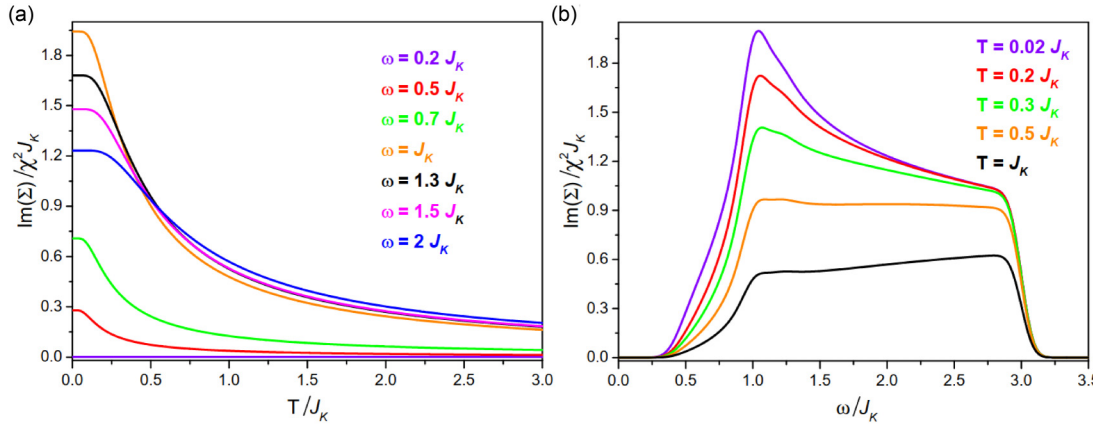

FIG. 16. Variation of phonon linewidth with (a) temperature and (b) frequency scaled with respect to the Kitaev coupling J_K.

where

$$G(\mathbf{k}, i\omega) = -\int_0^\beta d\tau \langle \mathcal{T} a_{\mathbf{k}}(\tau) a_{\mathbf{k}}^\dagger(0)\rangle_0 e^{i\omega\tau} = \frac{1}{i\omega - \epsilon_{\mathbf{k}}},$$
$$M_{\mathbf{k+q,k}} = \bar{\mathcal{A}}_{-\mathbf{q},\mathbf{k}}\bar{\mathcal{D}}_{\mathbf{q},-\mathbf{k}} + \bar{\mathcal{A}}_{-\mathbf{q},-\mathbf{k}-\mathbf{q}}\bar{\mathcal{D}}_{\mathbf{q},-\mathbf{k}} + \bar{\mathcal{D}}_{\mathbf{q},-\mathbf{k}}\bar{\mathcal{A}}_{-\mathbf{q},\mathbf{k}} + \bar{\mathcal{D}}_{\mathbf{q},\mathbf{k+q}}\bar{\mathcal{A}}_{-\mathbf{q},\mathbf{k}},$$
$$N_{\mathbf{k+q,k}} = \bar{\mathcal{B}}_{-\mathbf{q},-\mathbf{q}-\mathbf{k}}\bar{\mathcal{B}}_{\mathbf{q},-\mathbf{k}} + \bar{\mathcal{C}}_{-\mathbf{q},\mathbf{k}}\bar{\mathcal{B}}_{\mathbf{q},-\mathbf{k}} + \bar{\mathcal{B}}_{-\mathbf{q},\mathbf{k}}\bar{\mathcal{C}}_{\mathbf{q},-\mathbf{k}} + \bar{\mathcal{C}}_{\mathbf{q},\mathbf{k+q}}\bar{\mathcal{C}}_{-\mathbf{q},\mathbf{k}}.$$

To perform the Matsubara frequency summation, we define

$$I_1 = \lim_{R\to\infty} \frac{1}{2\pi i}\oint \frac{1}{e^{\beta z}+1}\frac{1}{z + i\omega + \epsilon_{\mathbf{k+q}}}\frac{1}{z - \epsilon_{\mathbf{k}}}, \tag{I5}$$
$$I_2 = \lim_{R\to\infty} \frac{1}{2\pi i}\oint \frac{1}{e^{\beta z}+1}\frac{1}{z + i\omega - \epsilon_{\mathbf{k+q}}}\frac{1}{z - \epsilon_{\mathbf{k}}}. \tag{I6}$$

Here, the contour is chosen to be a circle with radius R, and the radius is sent to ∞. The poles and residues of I_1 and I_2 are listed in Table II. Since, both the integrand vanishes as $R \to \infty$, therefore

$$-\frac{1}{\beta}\sum_{\omega_m}\frac{1}{i\omega + i\omega_m + \epsilon_{\mathbf{k+q}}}\frac{1}{i\omega_m - \epsilon_{\mathbf{k}}} = \frac{1 - n_F(\epsilon_{\mathbf{k+q}}) - n_F(\epsilon_{\mathbf{k}})}{i\omega + \epsilon_{\mathbf{k}} + \epsilon_{\mathbf{k+q}}},$$
$$\frac{1}{\beta}\sum_{\omega_m}\frac{1}{i\omega + i\omega_m - \epsilon_{\mathbf{k+q}}}\frac{1}{i\omega_m + \epsilon_{\mathbf{k}}} = \frac{n_F(\epsilon_{\mathbf{k}}) - n_F(\epsilon_{\mathbf{k+q}})}{i\omega + \epsilon_{\mathbf{k}} - \epsilon_{\mathbf{k+q}}}.$$

Hence

$$\Sigma(q, i\omega) \sim -\frac{\chi^2 J_K^2}{N_b}\sum_{\mathbf{k}}\Bigg[[1 - n_F(\epsilon_{\mathbf{k}}) - n_F(\epsilon_{\mathbf{k+q}})]\left(\frac{M_{\mathbf{k+q,k}}}{i\omega + \epsilon_k + \epsilon_{\mathbf{k+q}}} - \frac{M_{-\mathbf{k}-\mathbf{q},-\mathbf{k}}}{i\omega - \epsilon_{\mathbf{k}} - \epsilon_{\mathbf{k+q}}}\right)$$
$$+ [n_F(\epsilon_{\mathbf{k}}) - n_F(\epsilon_{\mathbf{k+q}})]\left(\frac{N_{\mathbf{k+q,k}}}{i\omega + \epsilon_{\mathbf{k}} - \epsilon_{\mathbf{k+q}}} - \frac{N_{-\mathbf{k}-\mathbf{q},-\mathbf{k}}}{i\omega + \epsilon_{\mathbf{k+q}} - \epsilon_{\mathbf{k}}}\right)\Bigg]. \tag{I7}$$

TABLE II. Poles and residues of I_1 and I_2.

I_1		I_2	
Poles	Residue	Poles	Residue
$i\omega_m$	$-\frac{1}{\beta}\sum_{\omega_m}\frac{1}{i\omega_m - \epsilon_{\mathbf{k}}} \times \frac{1}{i\omega + i\omega_m + \epsilon_{\mathbf{k+q}}}$	$i\omega_m$	$-\frac{1}{\beta}\sum_{\omega_m}\frac{1}{i\omega_m + \epsilon_{\mathbf{k}}} \times \frac{1}{i\omega + i\omega_m - \epsilon_{\mathbf{k+q}}}$
$\epsilon_{\mathbf{k}}$	$\frac{n_F(\epsilon_{\mathbf{k}})}{i\omega + \epsilon_{\mathbf{k}} + \epsilon_{\mathbf{k+q}}}$	$\epsilon_{\mathbf{k}}$	$\frac{n_F(\epsilon_{\mathbf{k}})}{i\omega + \epsilon_{\mathbf{k}} - \epsilon_{\mathbf{k+q}}}$
$-i\omega - \epsilon_{\mathbf{k+q}}$	$-\frac{1 - n_F(\epsilon_{\mathbf{k+q}})}{i\omega + \epsilon_{\mathbf{k+q}} + \epsilon_{\mathbf{k}}}$	$-i\omega + \epsilon_{\mathbf{k+q}}$	$-\frac{n_F(\epsilon_{\mathbf{k+q}})}{i\omega + \epsilon_{\mathbf{k}} - \epsilon_{\mathbf{k+q}}}$

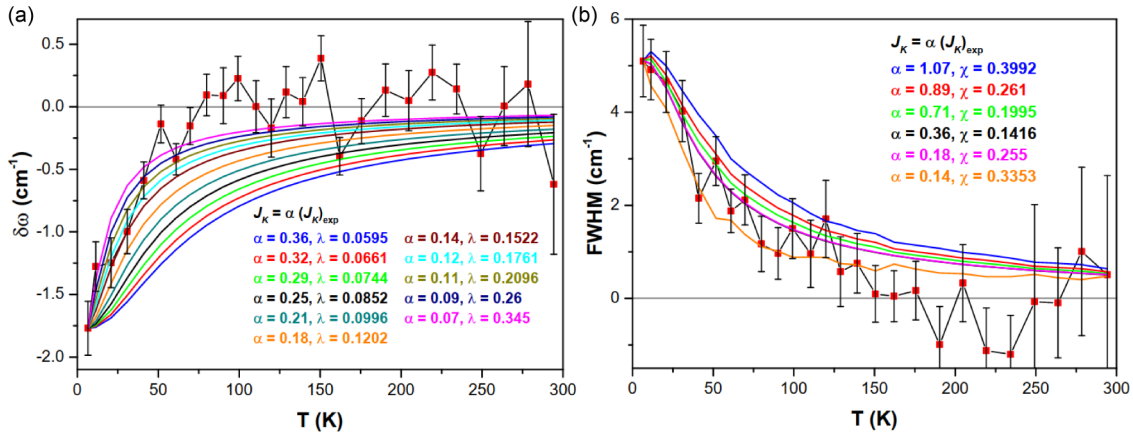

FIG. 17. Temperature dependence of (a) frequency shift and (b) FWHM for the M1 mode. Red squares are the experimental data after subtracting the anharmonic contribution. The smooth curves represent the theoretical curves at different values of the coupling constant. In (b), we plot only till $J_K = 40$ K considering the finite bandwidth ($\sim 3\ J_K$) effect as shown in Fig. 16(b).

In this paper, we consider the $\mathbf{q} \to 0$ limit, which is relevant to the Raman scattering. At this limit, the second part of the above expression with the factor $[n_F(\epsilon_{\mathbf{k}}) - n_F(\epsilon_{\mathbf{k}+\mathbf{q}})]$ vanishes. Finally, we Taylor-expand $M_{\mathbf{k}+\mathbf{q},\mathbf{k}}$ in powers of momentum and truncate the series up to the first nonzero term which is momentum independent. This gives the leading temperature dependence of the self-energy. We take the imaginary part of the above expression after doing the analytic continuation. Using the identity $\mathrm{Im}[\frac{1}{x-x_0+i0^+}] = -\pi\delta(x-x_0)$, we obtain

$$\mathrm{Im}[\Sigma(\mathbf{q},\omega+i0^+)] \sim \frac{\pi\chi^2 J_K^2}{N_b}\sum_{\mathbf{k}}[1-n_F(\epsilon_{\mathbf{k}})-n_F(\epsilon_{\mathbf{k}+\mathbf{q}})][\delta(\omega+\epsilon_{\mathbf{k}}+\epsilon_{\mathbf{k}+\mathbf{q}})-\delta(\omega-\epsilon_{\mathbf{k}}-\epsilon_{\mathbf{k}+\mathbf{q}})]. \tag{I8}$$

We further perform the momentum integral in Eq. (I8) numerically for $\mathbf{q} = 0$ considering the free fermionic dispersion to be $\epsilon_{\mathbf{k}} = 2|S(\mathbf{k})|$ [66].

The peak in Fig. 16(b) actually corresponds to the peak in the density of states of free Majoranas. In the experimental temperature regime, the flux excitations further renormalize the density of states. However, this does not change the qualitative features of Figs. 16(a) and 16(b). Note that the real part of Eq. (I7) also contributes to the renormalization of the frequency shift. However, we neglect this second-order contribution compared with Eq. (I2).

3. Fitting with free-Majorana calculation for the M1 mode

For completion we compare our free-Majorana results with the experiments for the M1 mode as shown in Fig. 17.

[1] P. W. Anderson, Science **177**, 393 (1972).
[2] R. B. Laughlin and D. Pines, Proc. Natl. Acad. Sci. USA **97**, 28 (2000).
[3] X. G. Wen, Rev. Mod. Phys. **89**, 041004 (2017).
[4] A. H. Castro Neto, F. Guinea, N. M. R. Peres, K. S. Novoselov, and A. K. Geim, Rev. Mod. Phys. **81**, 109 (2009).
[5] K. S. Novoselov, A. K. Geim, S. V. Morozov, D. Jiang, M. I. Katsnelson, I. V. Grigorieva, S. V. Dubonos, and A. A. Firsov, Nature (London) **438**, 197 (2005).
[6] X. Wan, A. M. Turner, A. Vishwanath, and S. Y. Savrasov, Phys. Rev. B **83**, 205101 (2011).
[7] B. Yan and C. Felser, Annu. Rev. Condens. Matter Phys. **8**, 337 (2017).
[8] N. P. Armitage, E. J. Mele, and A. Vishwanath, Rev. Mod. Phys. **90**, 015001 (2018).
[9] N. Read and D. Green, Phys. Rev. B **61**, 10267 (2000).
[10] C. Nayak, S. H. Simon, A. Stern, M. Freedman, and S. Das Sarma, Rev. Mod. Phys. **80**, 1083 (2008).
[11] F. Wilczek, Nat. Phys. **5**, 614 (2009).
[12] J. Alicea, Rep. Prog. Phys. **75**, 076501 (2012).
[13] A. Y. Kitaev, Phys.-Usp. **44**, 131 (2001).
[14] X. L. Qi and S. C. Zhang, Rev. Mod. Phys. **83**, 1057 (2011).
[15] S. Das Sarma, C. Nayak, and S. Tewari, Phys. Rev. B **73**, 220502(R) (2006).
[16] A. Das, Y. Ronen, Y. Most, Y. Oreg, M. Heiblum, and H. Shtrikman, Nat. Phys. **8**, 887 (2012).
[17] V. Mourik, K. Zuo, S. M. Frolov, S. R. Plissard, E. P. A. M. Bakkers, and L. P. Kouwenhoven, Science **336**, 1003 (2012).
[18] M. Banerjee, M. Heiblum, V. Umansky, D. E. Feldman, Y. Oreg, and A. Stern, Nature (London) **559**, 205 (2018).
[19] A. Kitaev, Ann. Phys. (Amsterdam) **321**, 2 (2006).
[20] Y. Kasahara, T. Ohnishi, Y. Mizukami, O. Tanaka, S. Ma, K. Sugii, N. Kurita, H. Tanaka, J. Nasu, Y. Motome, T. Shibauchi, and Y. Matsuda, Nature (London) **559**, 227 (2018).
[21] A. Banerjee, C. A. Bridges, J. Q. Yan, A. A. Aczel, L. Li, M. B. Stone, G. E. Granroth, M. D. Lumsden, Y. Yiu, J. Knolle, S.

Bhattacharjee, D. L. Kovrizhin, R. Moessner, D. A. Tennant, D. G. Mandrus, and S. E. Nagler, Nat. Mater. **15**, 733 (2016).
[22] G. Chen, A. Essin, and M. Hermele, Phys. Rev. B **85**, 094418 (2012).
[23] G. Jackeli and G. Khaliullin, Phys. Rev. Lett. **102**, 017205 (2009).
[24] Z. Nussinov and J. van den Brink, Rev. Mod. Phys. **87**, 1 (2015).
[25] J. G. Rau, E. K. H. Lee, and H. Y. Kee, Phys. Rev. Lett. **112**, 077204 (2014).
[26] K. Mehlawat, A. Thamizhavel, and Y. Singh, Phys. Rev. B **95**, 144406 (2017).
[27] S. H. Do, S. Y. Park, J. Yoshitake, J. Nasu, Y. Motome, Y. S. Kwon, D. T. Adroja, D. J. Voneshen, K. Kim, T. H. Jang, J. H. Park, K. Y. Choi, and S. Ji, Nat. Phys. **13**, 1079 (2017).
[28] A. Glamazda, P. Lemmens, S. H. Do, Y. S. Choi, and K. Y. Choi, Nat. Commun. **7**, 12286 (2016).
[29] A. Banerjee, J. Yan, J. Knolle, C. A. Bridges, M. B. Stone, M. D. Lumsden, D. G. Mandrus, D. A. Tennant, R. Moessner, and S. E. Nagler, Science **356**, 1055 (2017).
[30] S. M. Winter, A. A. Tsirlin, M. Daghofer, J. van den Brink, Y. Singh, P. Gegenwart, and R. Valentí, J. Phys.: Condens. Matter **29**, 493002 (2017).
[31] M. Abramchuk, C. Ozsoy-Keskinbora, J. W. Krizan, K. R. Metz, D. C. Bell, and F. Tafti, J. Am. Chem. Soc. **139**, 15371 (2017).
[32] Y. S. Choi, C. H. Lee, S. Lee, S. Yoon, W. J. Lee, J. Park, A. Ali, Y. Singh, J. C. Orain, G. Kim, J. S. Rhyee, W. T. Chen, F. Chou, and K. Y. Choi, Phys. Rev. Lett. **122**, 167202 (2019).
[33] E. M. Kenney, C. U. Segre, W. Lafargue-Dit-Hauret, O. I. Lebedev, M. Abramchuk, A. Berlie, S. P. Cottrell, G. Simutis, F. Bahrami, N. E. Mordvinova, G. Fabbris, J. L. McChesney, D. Haskel, X. Rocquefelte, M. J. Graf, and F. Tafti, Phys. Rev. B **100**, 094418 (2019).
[34] S. K. Takahashi, J. Wang, A. Arsenault, T. Imai, M. Abramchuk, F. Tafti, and P. M. Singer, Phys. Rev. X **9**, 031047 (2019).
[35] M. Ye, R. M. Fernandes, and N. B. Perkins, Phys. Rev. Res. **2**, 033180 (2020).
[36] M. Serbyn and P. A. Lee, Phys. Rev. B **87**, 174424 (2013).
[37] A. Metavitsiadis and W. Brenig, Phys. Rev. B **101**, 035103 (2020).
[38] K. Kitagawa, T. Takayama, Y. Matsumoto, A. Kato, R. Takano, Y. Kishimoto, S. Bette, R. Dinnebier, G. Jackeli, and H. Takagi, Nature (London) **554**, 341 (2018).
[39] F. Bahrami, W. L. D. Lafargue-Dit-Hauret, O. I. Lebedev, R. Movshovich, H. Y. Yang, D. Broido, X. Rocquefelte, and F. Tafti, Phys. Rev. Lett. **123**, 237203 (2019).
[40] R. Yadav, R. Ray, M. S. Eldeeb, S. Nishimoto, L. Hozoi, and J. van den Brink, Phys. Rev. Lett. **121**, 197203 (2018).
[41] Y. Li, S. M. Winter, and R. Valentí, Phys. Rev. Lett. **121**, 247202 (2018).
[42] J. Knolle, R. Moessner, and N. B. Perkins, Phys. Rev. Lett. **122**, 047202 (2019).
[43] S. Pei, L. L. Huang, G. Li, X. Chen, B. Xi, X. W. Wang, Y. Shi, D. Yu, C. Liu, L. Wang, F. Ye, M. Huang, and J. W. Mei, Phys. Rev. B **101**, 201101(R) (2020).
[44] F. Bahrami, E. M. Kenney, C. Wang, A. Berlie, O. I. Lebedev, M. J. Graf, and F. Tafti, Phys. Rev. B **103**, 094427 (2021).
[45] S. Sanyal, K. Damle, J. T. Chalker, and R. Moessner, Phys. Rev. Lett. **127**, 127201 (2021).
[46] Y. Motome and J. Nasu, J. Phys. Soc. Jpn. **89**, 012002 (2020).
[47] S. K. Choi, R. Coldea, A. N. Kolmogorov, T. Lancaster, I. I. Mazin, S. J. Blundell, P. G. Radaelli, Y. Singh, P. Gegenwart, K. R. Choi, S. W. Cheong, P. J. Baker, C. Stock, and J. Taylor, Phys. Rev. Lett. **108**, 127204 (2012).
[48] B. Perreault, J. Knolle, N. B. Perkins, and F. J. Burnell, Phys. Rev. B **92**, 094439 (2015).
[49] J. Nasu, J. Knolle, D. L. Kovrizhin, Y. Motome, and R. Moessner, Nat. Phys. **12**, 912 (2016).
[50] L. J. Sandilands, Y. Tian, K. W. Plumb, Y. J. Kim, and K. S. Burch, Phys. Rev. Lett. **114**, 147201 (2015).
[51] D. Wulferding, Y. Choi, S. H. Do, C. H. Lee, P. Lemmens, C. Faugeras, Y. Gallais, and K. Y. Choi, Nat. Commun. **11**, 1603 (2020).
[52] A. Glamazda, P. Lemmens, S. H. Do, Y. S. Kwon, and K. Y. Choi, Phys. Rev. B **95**, 174429 (2017).
[53] E. H. Hasdeo, A. R. T. Nugraha, M. S. Dresselhaus, and R. Saito, Phys. Rev. B **90**, 245140 (2014).
[54] G. Li, X. Chen, Y. Gan, F. Li, M. Yan, F. Ye, S. Pei, Y. Zhang, L. Wang, H. Su, J. Dai, Y. Chen, Y. Shi, X. W. Wang, L. Zhang, S. Wang, D. Yu, F. Ye, J.-W. Mei, and M. Huang, Phys. Rev. Mater. **3**, 023601 (2019).
[55] G. Li, L.-L. Huang, X. Chen, C. Liu, S. Pei, X. Wang, S. Wang, Y. Zhao, D. Yu, L. Wang, F. Ye, J.-W. Mei, and M. Huang, Phys. Rev. B **101**, 174436 (2020).
[56] J. Menéndez and M. Cardona, Phys. Rev. B **29**, 2051 (1984).
[57] P. G. Klemens, Phys. Rev. **148**, 845 (1966).
[58] L. Du, J. Tang, Y. Zhao, X. Li, R. Yang, X. Hu, X. Bai, X. Wang, K. Watanabe, T. Taniguchi, D. Shi, G. Yu, X. Bai, T. Hasan, G. Zhang, and Z. Sun, Adv. Funct. Mater. **29**, 1904734 (2019).
[59] J. Nasu, M. Udagawa, and Y. Motome, Phys. Rev. B **92**, 115122 (2015).
[60] S. J. Allen and H. J. Guggenheim, Phys. Rev. B **21**, 1807 (1968).
[61] N. Suzuki and H. Kamimura, J. Phys. Soc. Jpn. **35**, 985 (1973).
[62] A. J. Willans, J. T. Chalker, and R. Moessner, Phys. Rev. Lett. **104**, 237203 (2010).
[63] A. J. Willans, J. T. Chalker, and R. Moessner, Phys. Rev. B **84**, 115146 (2011).
[64] R. Bhola, S. Biswas, Md M. Islam, and K. Damle, arXiv:2007.04974.
[65] S. Bhattacharjee, S. Zherlitsyn, O. Chiatti, A. Sytcheva, J. Wosnitza, R. Moessner, M. E. Zhitomirsky, P. Lemmens, V. Tsurkan, and A. Loidl, Phys. Rev. B **83**, 184421 (2011).
[66] J. Knolle, S. Bhattacharjee, and R. Moessner, Phys. Rev. B **97**, 134432 (2018).
[67] A. N. Ponomaryov, L. Zviagina, J. Wosnitza, P. Lampen-Kelley, A. Banerjee, J.-Q. Yan, C. A. Bridges, D. G. Mandrus, S. E. Nagler, and S. A. Zvyagin, Phys. Rev. Lett. **125**, 037202 (2020).
[68] S. Bachus, D. A. S. Kaib, Y. Tokiwa, A. Jesche, V. Tsurkan, A. Loidl, S. M. Winter, A. A. Tsirlin, R. Valentí, and P. Gegenwart, Phys. Rev. Lett. **125**, 097203 (2020).
[69] A. Metavitsiadis, W. Natori, J. Knolle, and W. Brenig, arXiv:2103.09828.
[70] Y. Yang, M. Li, I. Rousochatzakis, and N. B. Perkins, Phys. Rev. B **104**, 144412 (2021).